Geothermal Play-Fairway Analysis of Washington State Prospects: Phase 2 Results

Corina Forson[1], Alexander N. Steely[1], Trenton Cladouhos[2], Mike Swyer[2], Nicholas Davatzes[3], Megan Anderson[4], Brent Ritzinger[5], Jonathan Glen[5], Jared Peacock[5], William Schermerhorn[6], Erick Burns[7], and Pete Stelling[6]

[1]Washington Geological Survey
Department of Natural Resources , MS 47007
Olympia, WA 98504-7007

[2]AltaRock Energy, Inc.
4010 Stone Way North, Suite 400
Seattle, WA 98103

[3]Temple University
1901 N. 13th St
Philadelphia, PA 19122

[4]Colorado College
14 E. Cache La Poudre St
Colorado Springs, CO 80903

[5]US Geological Survey
345 Middlefield Road, MS 989
Menlo Park, CA 94025

[6]Western Washington University
516 High St, MS 9080
Bellingham, WA 98225

[7]US Geological Survey
Oregon Water Science Center
2130 SW 5th Ave
Portland, OR 97201

Keywords

Play-fairway, Washington State, Mount Baker, Mount St. Helens, Wind River Valley, heat potential, permeability potential, infrastructure potential, exploration risk, fluid-filled fracture potential, geothermal modeling, Poly3D, geophysics, geologic mapping.

ABSTRACT

An investment of $0.7M from the Geothermal Technology Office for Phase 2 of Play Fairway Analysis in Washington State improved existing favorability models and increased model confidence. The new 1:24,000-scale geological mapping, 15 detailed geophysical surveys, 2 passive seismic surveys, and geochronology collected during this phase are coupled with updated and detailed structural modeling and have significantly improved the conceptual models of three potential blind geothermal systems/plays in Washington State: the St. Helens Shear Zone, Mount Baker, and Wind River Valley. Results of this analysis reveal the presence of commercially viable undiscovered geothermal resources in all three study areas. The analysis additionally provides a clear definition of the geothermal prospects in terms of the essential elements of a functioning geothermal system, the confidence in these assessments, and associated potential and risk of development. As a result, several groups have recently approached our organization about opportunities for large-capital moderate- to high-temperature geothermal development and are very interested in the results of Phase 3 drilling. Our updated models, coupled with development interest, provides a compelling basis for investment in future validation activities.

1. Introduction

1.1. Washington Geothermal Play Fairway

The Washington State Geothermal Play is conceptually simple; heat is provided by the injection of magma at shallow crustal levels along the active Cascade volcanic arc and permeability is provided by an extensive network of steep active faults that can effectively transfer heat from deeper sources to reservoirs near the surface. Abundant seismicity, Quaternary crustal shortening between Oregon and Canada (Stanley and others, 1996; McCaffrey and others, 2007), and historic and Holocene fault ruptures (e.g. Bucknam and others, 1992; Personius and others, 2014) provide evidence of active tectonics. Hot springs and fumaroles exist around some of the volcanic centers in the state but the extreme precipitation—over 3 m/yr along much of the Cascade Range—and dense vegetation has likely suppressed the surface expression of geothermal systems in many areas.

Three areas were selected for further study in Phase 1 (Fig. 1) based on the results of a statewide geothermal assessment (Boschmann and others, 2014): the Mount Baker region (MB), the areas north and south of Mount St. Helens (MSH) within the St. Helens shear zone (SHSZ), and the Wind River Valley (WRV). The updated conceptual models for each of these areas (Fig. 2) are provided up-front to provide context for the data sets and favorability models that follow. Common to each conceptual model are the defining characteristics of a geothermal system: a source of heat, a pathway for heat movement—typically aided by channeled fluid flow along portions of active faults, and a shallow, accessible heat reservoir kinematically maintained within an active fracture network. This whole-system approach promotes the effective transfer of knowledge between similar plays while still allowing for individual differences based on local conditions.

The goal of the Play Fairway Analysis (PFA) in Washington has been to develop a method that effectively identifies favorable regions of enhanced permeability near viable heat sources with

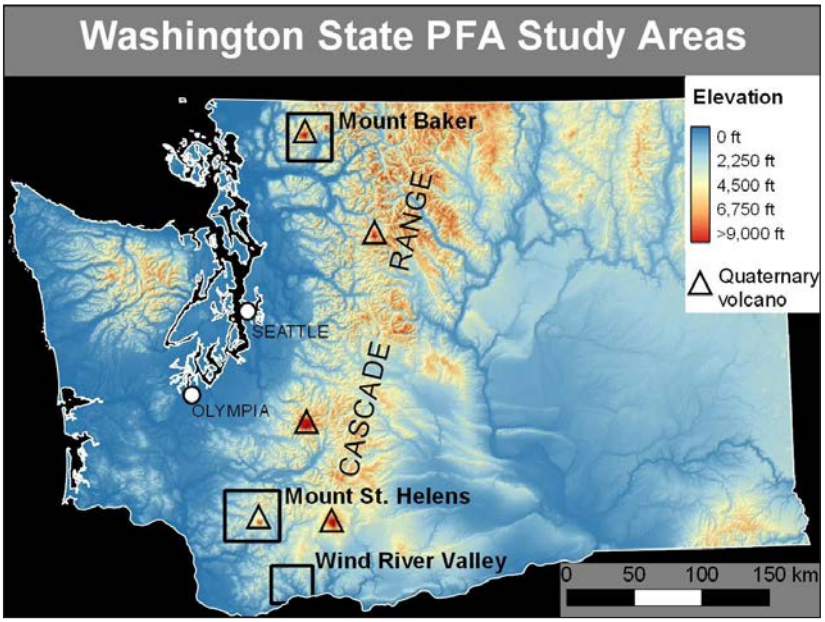

Figure 1. Locations of study areas in Washington State.

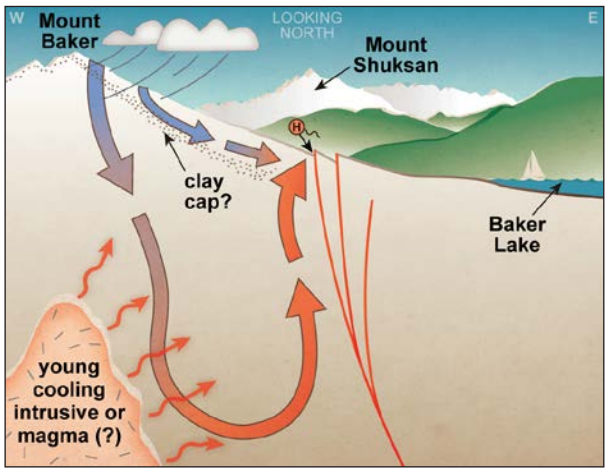

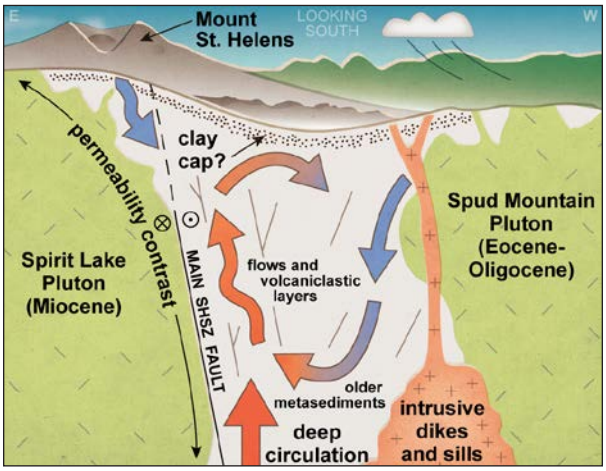

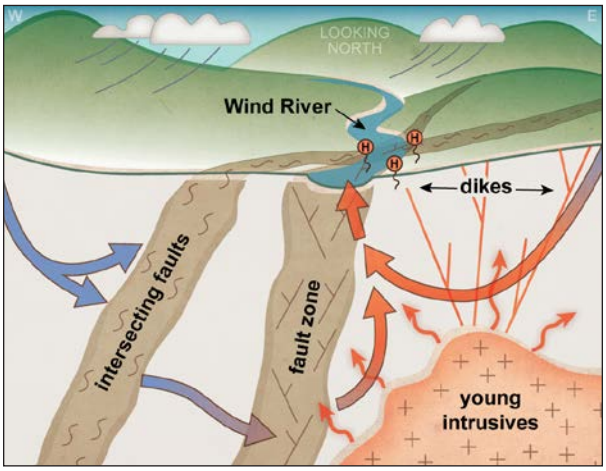

Figure 2. Updated conceptual models for Mount Baker (left), Mount St. Helens (below left), and Wind River Valley (below). Abundant Quaternary volcanism provides heat; active deformation along faults and fractures provides permeable pathways for the convection of geothermal fluids. Models are not to scale; viewing directions are provided in white at the top of each figure.

the intention of supporting commercial exploration and development of the region. Washington State has a mandate to source 15% of its energy portfolio from renewable sources by 2020; the state's largest source of energy is currently hydro-electric which does not qualify as 'renewable' by the Energy Independence Act (I-937).

1.2. Summary of Phase 2 Activities

1.2.1. Data Collection

To support the aims of the Geothermal Technology Center during Phase 2 of Play Fairway Analysis, nearly $1M in geophysical and geologic data collection was proposed. All funded activities (Table 1) were completed on time, within scope, and on or under budget. Additionally, this project benefited from activities performed beyond the scope of work (geophysical modeling of 2D cross sections and lidar acquisition) at no cost. Brief summaries of major relevant findings are presented in the following sections; detailed reports for each activity will be included in the final technical document at the conclusion of the Phase 2 performance period.

1.2.2. Revised Favorability And Confidence Modeling Methods

A revision of the Phase 1 methods was required to effectively incorporate the data collected during Phase 2. These improvements focused on the development of a more-robust method to evaluate model confidence, characterize potential heat sources, and evaluate the likelihood of encountering fluid-filled fractures at depth. Two new models were developed: a fluid-filled fracture potential model, which is incorporated into the final geothermal model, and an infrastructure model that systematically addresses issues related to the viability of siting, permitting, and drilling. A summary of these improvements is provided in the sections below and a more-detailed description will be available in the final Phase 2 report.

Table 1. Summary of proposed, funded, and completed activities. Solid circles indicate requested, funded, and completed; hollow circles indicate requested but not funded; plus signs indicate activities completed at no cost to the project; dashes indicate not requested.

Method	Mount Baker (MB)	North of Mount St. Helens (MSH-N)	South of Mount St. Helens (MSH-S)	Wind River Valley (WRV)
1:24,000-scale geologic mapping	●	●	○	Compl. 2014
Lidar collection (opportunistic) and interpretation	+	+	+	+
Magneto-telluric survey (MT)	●	●	●	– – –
Passive seismic surveys	– – –	●	○	– – –
Ground-based gravity survey	●	●	●	●
Ground-based magnetic survey	●	●	●	●
2D modeled cross sections using using geology and potential fields	+	+	+	+
Aeromagnetic survey	– – –	– – –	– – –	○
Geochronology	– – –	●	– – –	●
Electrical resistivity survey	●	●	○	Compl. 2014
Temperature-gradient well	○	– – –	– – –	– – –

1.2.3. Updated Model Weights Using The Analytical Hierarchy Process

The weights of individual layers within a model—and the contribution of each model to the final geothermal potential—are calculated using a consensus-based expert opinion approach

known as the Analytical Hierarchy Process (AHP)(Saaty, 2008; Goepel, 2013). The AHP is implemented as an Excel spreadsheet and helps groups make complex decisions by having each participant rank input layers as a series of pair-wise comparisons with weights that determine the strength of the comparison. The spreadsheet informs the participants how consistent their choices and weights are. Ultimately, the layer weights are tabulated and calculated based on the input from all participants. For Phase 2 there were 8 to 10 participants consisting of two geologists from DNR, two geologists from AltaRock Energy, four geologists and geophysicists from the USGS, two geologists from academic institutions, and one hydrologist from the USGS.

2. Revised And New Modeling Methods

2.1. Heat

2.1.1. Justification Of Improvements

A critical element of predicting geothermal potential is derived from the Play-Fairway heat model. It is this component of prediction that is most easily tested with temperature-gradient exploratory drilling. Because of this strong predictor/validation relationship we chose to evaluate and update the Phase 1 modeling approach. Based on other team's Phase 1 reports, and a more-extensive literature review, we were able to identify and remedy several key shortcomings of our Phase 1 model approach, as summarized below. These changes required correlative updates to the confidence models. A detailed description of methods and intermediate data layers will be available in the final technical report; a brief description is provided below.

2.1.2. Favorability Modeling

Model scope: The improved method models the entire state of Washington and clips the final results to each study area instead of modeling each study area individually. Such a step was made possible by the comprehensive geological databases developed by the Washington Geological Survey and removes the need to assign arbitrary boundary conditions at the edge of each study area. This approach also expedites modeling of the remainder of the state once Phase 3 validation results become available.

Continuous instead of discrete: A major refinement was initiated after reviewing how temperature observations (springs, wells, geothermometry) were integrated into the model. In Phase 1, each observation—such as a temperature-gradient well—was given a small 'radius of influence' on the order of a few hundred m. Within this region, favorability could range from low to high depending on the value of the observation; outside of the small region the favorability was zero. This had two effects: (1) it gave our temperature-observation layers a 'spotted' appearance, and (2) it biased the favorability estimate by only having values very close to existing data. In effect, this approach made it impossible to predict values at distance from point observations.

An alternative approach adopted for Phase 2 is to model the three temperature observation layers as continuous fields of predicted values which are algorithmically determined from available observations. In this way we can then predict, for example, the temperature of a well at any location instead of biasing favorability towards existing data. This change required a robust approach to

interpolation and attention to data quality for each observation guiding the interpretation. To this end, we employed the nonparametric inverse-distance weighting (IDW) method and added the ability to weight each observation based on a set of quality criteria. For each layer we briefly outline the weighting and scaling strategy below.

Table 2. Summary of heat potential raster scaling.

Data layer	Criteria	Value
Subsurface temperature observations	<20°C/km >60°C/km	0 1
Springs	<10°C >75°C	0 1
Quaternary volcanic vents	Proximity weighted by age and vent type	0 1
Quaternary intrusive rocks	Proximity weighted by age	0 1
Geothermometry	<20°C >120°C	0 1

Layer weights and scaling: Each input layer has different data-quality parameters or uncertainty metrics which are used to weight their influence on the prediction and are discussed in the section below. Table 2 indicates the scaling used to convert the data from measured values to a common 0–1 rank that can then be combined according to weights determined by AHP for each data type.

Subsurface temperature observations (wells)—The weighting scheme from Phase 1 was modified to retain the well type and well depth ranking so that deep temperature-gradient wells are weighted more heavily than shallow wells with only a bottom-hole temperature (Table 3). The ranking by number of temperature measurements was moved into the confidence model.

Table 3. Weights for subsurface temperature observation layer.

Well type	Depth (m)	Weight
Well with bottom-hole temperature only	any	0.25
Temperature-gradient	0–100	0.5
Temperature-gradient	100–250	0.75
Temperature-gradient	>250	1

Springs—No weighting was performed on these data in either Phase 1 or Phase 2.

Geothermometry—No weighting of these data was performed in Phase 1, yet there are clear quality indicators which affect observation validity and should be considered. A weighting scheme was developed that uses charge balance, vintage of analysis (average for repeat surveys), and internal consistency between thermometer systems. Each of these rankings was then weighted and combined to determine the overall rank for the observation (Table 4).

Quaternary volcanic vents—In Phase 1, this layer employed a variable-distance buffer around different vent types. For Phase 2 the buffer size was improved to better capture the correlation between vent proximity and cumu-

Table 4. Favorability weights for geothermometry layer.

Indicator	Criteria	Value	Weighting
Charge balance	<3% >12%	1 0	0.5
Inter-method discrepancy	<15°C >100°C	1 0.2	0.25
Year of analysis	>2000 <1975	1 0.5	0.25

lative geothermal prospects in a similar volcanic-arc play (Indonesia) where ~85% of prospects are within 8 km of a stratovolcano and 95% are within ~16 km (Carranza and others, 2008). We used this data to set a favorability window around stratovolcanoes of 100% up to 8 km that decreases linearly to 0% at 16 km. Smaller buffers (with identical ratios) are used for the remaining types of volcanic vents.

Table 5. Favorability weights for Quaternary volcanic vents layer.

Buffer size and gradient distance		
Vent type	**100% value distance**	**Linear gradient distance**
Stratovolcano	0 to 8 km	8 to 16 km
Calderas, domes, plugs	0 to 5 km	5 to 10 km
Minor vents and cinder cones	0 to 2.5 km	2.5 to 5 km

Age weighting	
Criteria	**Rank**
<160 ka	1
160–780 ka	0.75
780–2,500 ka	0.5

Phase 1 also employed a tiered age/composition ranking for volcanic vents that created a 14x range in favorability between the most and least favorable combination with little statistical basis for such an extreme range. Although there is a common perception in the geothermal community that high magma viscosity is a strong predictor of stored shallow-crustal volcanogenic heat, a robust global statistical analysis from the Alaska Phase 1 Play Fairway Analysis does not support such a relationship. On this basis, the 14x range in favorability from our Phase 1 method seems unsupportable by available data and we removed the composition ranking completely. The remaining ranking is based entirely on age and distance from a heat source (Table 5).

Quaternary intrusive rocks—No changes were implemented to weighting or buffer size.

2.1.3. Confidence Modeling

Observations of temperature: In Phase 1, the confidence modeling focused entirely on observation uncertainty (accuracy of results and location accuracy). This approach was satisfactory because observations were modeled as discrete points with buffers in-stead of a continuous predictive surface. In Phase 2 we introduce two additional components of confidence modeling: (1) the misfit between input observations and the predictive surface, and (2) the proximity to the nearest observation (which replaces the Phase 1 observation buffer). The final result is a continuous estimate of confidence that accounts for the map-view distribution of observations, their individual uncertainty or weighting, and the ability of the predictive model to fit the observations.

The model misfit is characterized using a goodness-of-fit function that is the complement of the relative misfit: GOF=1-((O-P))/P where O is the observed value and P is the predicted value from the interpolated surface. This is multiplied by the weighting scheme (discussed above) of the respective data layer to arrive at an intermediate confidence value which characterizes the model misfit and the observation's weight. Table 6 shows the subsurface temperature observation layer as an example.

To account for the uneven map-view distribution of observations we use a gaussian kernel density estimation (KDE) technique with a 10-km radius. Conceptually, this approach treats areas with

abundant observations as better-known (more confident) than areas with fewer or no observations. We account for the effect of variable observation confidence (model misfit and observation weight) by weighting the KDE by our intermediate confidence value.

Table 6. Confidence weights for subsurface temperature observation layer use the goodness-of-fit multiplied by the observation weight.

		GOF (complement of relative misfit)		
		perfect match between model and observation		more than 50% misfit between model and observation
		1	0.75	0.5
Observation weight	1	1	0.75	0.5
	0.75	0.75	0.5625	0.375
	0.5	0.5	0.375	0.25
	0.25	0.25	0.1875	0.125

Observations from geologic maps: The Phase 1 method considered the number of mapped-vent citations and whether the vent had associated geochronology. An example highlights the need for improvement—using the Phase 1 method, new 1:24,000-scale geologic mapping that identified a volcanic vent and used nearby well-dated stratigraphy to constrain its relative age to 10–40 ka would have been ranked poorly whereas a vent mapped in the 1950s and then compiled at a 1:100,000 scale in the 1970s would be ranked highly. This approach does not adequately reflect the information most valuable to assessing confidence, namely: (1) how certain is a mapped feature and its age assignment, and (2) how certain is the absence of a mapped feature (does it reflect an actual absence of the feature or a cursory mapping campaign)?

In Phase 2 the modeling was revised to include the scale and vintage of mapping and the proximity to available geochronology (Table 7). The scale of mapping is likely to be a better predictor of mapping quality than the number of sources for a particular feature because it also addresses the issue of certainty in what was not observed. The vintage of mapping is a justified addition because the advent of DEMs in the early 2000s and abundant lidar in the 2010s has greatly aided in identification and characterization of young volcanic features. Proximity to geochronology is a better predictor of vent-age confidence because it acknowledges that meaningful constraints on the age of a feature can be found in understanding the regional or sub-regional stratigraphy. To these ends, we use the extent of the best-available mapping in our study areas, weighted for scale of mapping and vintage, and combine this with a KDE of post-latest Miocene geochronology (Table 8) that could be useful in determining the age of Plio-Pleistocene volcanic and intrusive rocks.

Table 7. Confidence weights for scale and age of mapping (60% of vent confidence layer).

		Vintage of mapping		
		Since 2010	2010-2000	Before 2000
Scale of mapping	**Weights**	1	0.9	0.8
1:24,000 or better	1	1	0.9	0.8
1:24,000 to 1:100,000	0.9	0.9	0.81	0.72
1:100,000	0.8	0.8	0.72	0.64

Table 8. Confidence weights for age of volcanic vent (40% of vent confidence layer).

Age of observation	Weight
0–160 ka	1
160–780 ka	0.75
780–2,500 ka	0.5
2.5–23 Ma	Linear ramp from 0.25 to 0

2.2. Permeability

2.2.1. Justification Of Improvements

A substantial portion of Phase 2 activities were aimed at improving fault geometry and subsurface characterization; five main changes were implemented in the favorability modeling to highlight these improvements: (1) updated material properties, (2) addition of seismicity and fault density layers, (3) removal of four low-weight Phase 1 layers, (4) refined high-resolution *Poly3D* modeling, and (5) updated study-area-wide slip and dilation tendency modeling. Additional changes to the confidence modeling were required to adequately assess improvements gained through the collection of new data. Detailed descriptions of method improvements and intermediate raster layers will be available in the final Phase 2 report; brief descriptions are provided below.

2.2.2. Favorability Modeling

Material properties in the *Poly3D* model (Poisson's ratio and Young's modulus) were updated using a combination of geophysical observations in the study areas and lithology-specific values from literature (Table 9); these values were assumed to be invariant during Phase 1 modeling. Values of Poisson's ratio were constrained at MSH-N from the Vp/Vs ratio determined from earthquake passive-seismic tomography using the equation $\upsilon=(1(Vp/Vs)-2)/(2(Vp/Vs)-1)$. Values of Vp/Vs were averaged in the NW-trending region between the Spirit Lake and Spud Mountain plutons from 0 to 2 km depths for use in this calculation; a Young's modulus was chosen that was appropriate for Neogene marine sediments and volcaniclastics (Waite and Moran, 2009; Zhu, 2012). Values from representative lithologies for the other study areas (Schultz, 1993; Tabor and others, 2003; Zhu, 2012) were chosen and used in the modeling.

Table 9. Poisson's ratio and and Young's modulus for Poly3D models.

Study area	Poisson's ratio	Young's modulus (GPa)	Dominant modeled lithology
Mount Baker	0.21	20	Cretaceous argillite
Mount St. Helens	0.3	20	Neogene volcaniclastics
Wind River Valley	0.25	57	Neogene basalt

Seismic-event density and fault density were added as model inputs. Seismicity was implicitly considered in some study areas during Phase 1 by informing the modeled fault geometries; its addition in Phase 2 provides a mechanism to explicitly include it. The density kernel assigns a value of 0 to regions with <1 event/km^2 and a value of 1 to regions with >4 events/km^2. These values were selected because they highlight regions with abundant seismicity and show prominent linear trends associated with major known active fault zones (see Figures 3, 4, and 6).

The addition of a fault-density layer is conceptually justified by the idea that permeability will generally be higher where there are closely spaced or intersecting faults (Curewitz and Karson, 1997). The new surface mapping and lidar interpretation—coupled with subsurface characterization of fault geometries—provided updated fault maps at each study area (at the 200-m and 2-km depths) which were used for the calculation. Each fault segment was converted to points with ~30-m spacing; a gaussian kernel density estimator with 500-m radius was used and the results were scaled so that a value of 0 means no nearby fault, 0.5 is a single fault strand, and a value

of 1 indicates at least two faults in very close proximity or intersecting. The radius of influence (500 m) is a favorable interpretation of the upper limit of increased fracture density from a moderate-size fault (Johri, 2012).

Several Phase 1 model inputs were not considered in the Phase 2 model: fault-displacement distribution, tensile-fracture density, regional-scale maximum shear-strain rate, and surface dilational strain rate. All four inputs were weighted low in Phase 1; the first two largely duplicate other model outputs and the last two did not provide much discrimination power either between study areas or within them. The goal of this change was to reduce model complexity while retaining enough information to assess and predict the variations in normal traction on fault surfaces as a result of regional strain and local stress perturbations along major faults.

A focused *Poly3D* model area was selected at each of the AOIs and run with a significantly higher resolution using a simplified version of the updated fault models. Refined model areas were chosen to overlap the regions of new data collection; node spacing was improved from 305 m to 100 m in order to capture the finer-scale fault structures elucidated during Phase 2 field activities. *Poly3D* is a boundary-element model that characterizes both on- and off-fault deformation resulting from sub-regional strain and from slip along large-scale active structures (Thomas, 1993). Major structures are used to 'drive' the stress/strain field and the smaller-scale structures 'respond' to the imposed conditions. Major structures were selected from the updated fault model using at least two of the following criteria: collocation of seismic events on fault planes, collocation of faults with appropriately oriented focal mechanisms, collocation of faults with major potential-field boundaries (gravity, MT, seismic velocities), and collocation of faults with abundant field evidence of activity (lidar lineaments along well-mapped and observed faults). A detailed discussion of the *Poly3D* modeling assumptions and methods is available in the Phase 1 report; a detailed update of model parameters and selected faults will be available in the final Phase 2 report.

In addition to the refined modeling, a 2D slip and dilation tendency model was run for all faults in the study areas. The numerical limitations of the *Poly3D* software preclude its use on high-resolution model domains at scales appropriate for an entire study area. The addition of the computationally simpler slip- and dilation-tendency allows us to also refine permeability potential outside of the smaller AOIs. This approach is sub-optimal because regions outside of the refined *Poly3D* model lack some outputs—and thus have slightly lower favorability. However, this limitation is less relevant than it seems because nearly all of the proposed drill sites fall within the regions with refined *Poly3D* models. The slip and dilation tendency model produces scaled favorability for each fault segment; each segment was then buffered with its corresponding value to a distance of 250 m based on the extent of simulated damage zone caused by faults and fault intersections in the *Poly3D* models.

2.2.3. Confidence Modeling

The collection of six new data sets during Phase 2 (and the addition of existing aeromagnetic data) was a challenge to the Phase 1 uncertainty model which was built to only consider the two data sets that were used at that time. The new data have greatly clarified the location and geometry of faults and the likely permeable pathways; thus a revised confidence model was developed

Table 10. Confidence weighting scheme for permeability model in Phases 1 and 2.

Phase 1		Phase 2			
			Relative weight in construction of Phase 2 fault geometry		
Inputs	Relative weight in construction of Phase 1 fault geometry	Inputs	MB	MSH	WRV
Mapped faults	0.50	Mapped faults (with new mapping) and fault observations (kinematics or orientation)	0.10	0.35	0.30
Seismicity	0.50	Seismicity	0.05	0.20	0.07
– – –	– – –	Detailed gravity surveys	0.13	0.15	0.26
– – –	– – –	Aeromagnetic surveys (all areas) and ground-based magnetic survey (MB only)	0.33	0.08	0.10
– – –	– – –	2D modeled cross-sections	0.16	0.10	0.10
– – –	– – –	Lidar interpretation	0.22	0.15	0.17

to document the reduction in uncertainty. Because the permeability modeling requires two main inputs—stress/strain boundary conditions and fault geometry—and only fault geometry was substantially modified during Phase 2, the confidence model focuses on these changes. Additionally, the tensor algebra used in the modeling ensures that confidence is transitive; that is, an increase in confidence of an input parameter also increases the confidence of the model results.

One of the advantages of our method is that it provides a mechanism to vary the weighting of a particular data set within a more general framework. For example, seismicity was much less influential in constraining fault geometry in the Wind River Valley than at Mount St. Helens, and ground-based magnetic surveys were only available at Mount Baker (Table 10). Because of these differences, separate AHP values were calculated for each study area.

Layer weights and scaling:

Mapped faults and fault observations—Conceptually, confidence is high where mapped faults are certain and there are abundant observations of fault kinematics or orientation. A layer was created that combines proximity to mapped faults (weighted by type) and density of fault observations. Relevant parameters are provided in Table 11.

Seismicity—A high density of seismic events can be used to delineate the geometry of active faults in the subsurface, such as along the SHSZ. Fault geometries at depth in regions that lack a large number of events are more uncertain. A layer of seismic event density was developed using the entire catalogue of relocated seismicity in Washington from Czajkowski and Bowman (2014). The layer was scaled so that <1 event/km^2 was a confidence value of 0, and >4 events/km^2 was a confidence value of 1.

Gravity and Magnetics—Regions with high station density or closely spaced flight lines have tighter constraints on

Table 11. Intermediate weights and scaling for fault and fault-observation confidence layers.

Data type	Criteria	Scaling	Radius	Layer weight
Mapped faults	Certain Approximate Inferred Concealed Querries	1.0 0.75 0.5 0.25 0.10	250 m	0.6
Fault observations	0 obs/km^2 ≥1 obs/km^2	0 1	250 m	0.4

Table 12. Intermediate weights and scaling for gravity survey confidence layers.

Target interpretation depth	Criteria	Scaling	Radius	Layer weight
Near-surface	<0.7 station/km^2 >5 stations/km^2	0 1	500 m	0.5
1–3 km	0 stations/km^2 1 station/km^2	0 1	2.5 km	0.5

the shape and character of the potential field than areas with sparse coverage. For gravity-field surveys, two station density maps were combined into a single confidence layer: one with a short radius to highlight areas with good near-surface constraints (0–2 km depth) and another with a larger radius to show areas with good resolving power at 2–10 km depths (Table 12). For magnetic-field surveys, a single confidence layer was constructed using either the proximity (<500 m) to aeromagnetic flight lines or ground-based magnetic survey lines, whichever had the higher resolution. This approach does not explicitly account for the direction of the flight lines relative to the potential-field gradient—structures perpendicular to flight lines are better constrained than those that are parallel.

Modeled cross sections—A major component of Phase 2 activities was the development of 10 potential-field-constrained 2D cross-sections. Hand samples were collected from all major lithologies in the study areas and magnetic susceptibility and density were measured. Each cross section uses available geologic mapping and models the expected gravity and magnetic field at the surface and compares with the observed values. In this way the cross sections can be iteratively refined to develop a subsurface interpretation that is geologically based and produces a close fit between the predicted and observed potential fields. A confidence layer was developed using the proximity (<1.5 km) to these cross section lines.

Lidar—The opportunistic collection of lidar at all of our study areas is a huge benefit for Phase 2 activities: it was used to identify potentially active faults at all three study areas and served as a base map for new 1:24,000-scale mapping at MSH. Many of the newly identified lineaments are collocated with mapped faults, fault observations, steep potential-field gradients, boundaries in the MT data, and bands of seismicity. A simple confidence layer was developed using proximity (<250 m) to mapped lidar lineaments.

2.3. Fluid-Filled Fractures

2.3.1. Justification Of Addition

The Phase 1 modeling did not assess the likelihood of encountering fluid-filled fractures in the subsurface. Based on feedback from the Play-Fairway Technical Monitoring Team—and with the addition of new data—this important aspect was more fully considered during Phase 2 (Table 13). Conceptually, large contiguous volumes of fluid-filled fractures are more likely to have permeable pathways that allow convective circulation; these regions also provide a reservoir for geothermal heat. Four data sets were used to develop this model—although not all are available in each study area: (1) resistivity models from magnetotelluric data, (2) Vp/Vs ratios from earthquake tomography, (3) shear wave velocities (Vs) from ambient-noise tomography, and (4)

density of seismic events. These data can also be compared for internal consistency with independent outputs of the permeability potential model such as the maximum coulomb stress (which can be interpreted to predict fracture density). A brief overview of how these data were used in the model is provided be-low; more-detailed method descriptions will be provided in the final Phase 2 report.

Table 13. Summary of fluid-filled fracture layer scaling and availability.

Data layer	Criteria	Scaling	Availability
Resistivity (Ω-m)	<10 >300	0 1	MB, MSH-N, MSH-S
Vp/Vs (unitless)	<1.6 >1.9	0 1	MSH-N
Vs (ambient-noise) (km/s)	<2 >4	0 1	MSH-N
Seismic-event density (events/km^2)	<1 >4	0 1	All

2.3.2. Favorability Modeling

Highly conductive anomalies in MT data are often associated with warm fluid-filled fractures and reservoirs in geothermal systems (e.g. Coso geothermal field; Wannamaker and others, 2004). Such features are interpreted in the resistivity data in all three areas (MB, MSH-N, and MSH-S) and are discussed in the Results of New Data Collection section. However, geophysical properties generally have a non-unique relationship to the presence of fluids since other factors such as salinity, temperature, rock type, and fracture density also play a role. Where possible, this is addressed by combining multiple independent geophysical properties with differing dependencies. The result is improved confidence in the model of fluid favorability.

High Vp/Vs ratios can indicate regions of fluid-filled fractures, because shear waves are slowed more by pore fluid then compressive waves (O'Connell and Budiansky, 1974; Lees and Wu, 2000). Currently the Vp and Vs layers are inverted separately, which could lead to Vp/Vs artifacts; although no obvious artifacts were noted in the current data set. To provide more robust Vp/Vs maps a joint inversion is being performed and will be presented in the final Phase 2 report.

The density of seismic events was included in this model because earthquakes are indicative of subsurface deformation and their presence is a predictor of processes that facilitate fracturing and promote high fracture density. Because seismic-station density is insufficient to accurately assess the depth of events <2–5 km in all of the study areas, the map-view density of events is used.

2.3.3. Confidence Modeling

The approach to assessing confidence in the MT layer follows the general premise used elsewhere: use the density of observation points and weight them by a quality or uncertainty value. For the MT data, a gaussian kernel-density estimator of stations with a 2 km radius was used and each station was weighted by its relative root-mean-square error. In this way, confidence is highest where stations are closely spaced and the resistivity-model errors are low; confidence is low where model errors are high or where stations are sparse.

The passive-seismic datasets both provide an uncertainty value for each pixel in the model that accounts for station density and so a KDE was not used. Uncertainty in the earthquake tomography Vp and Vs data is a function of the combined length of raypaths that traversed the pixel and the uncertainty in arrival time. Values from both Vp and Vs were summed in quadrature and the

result was scaled so that a confidence value of 0 indicates no raypaths through the pixel in either model and a value of 1 indicates 4 raypaths per pixel (although the raypath length can be distributed unevenly between the Vp and Vs models). The ambient-noise Vs layer used the uncertainty in phase-velocity at each pixel and was scaled so that a confidence value of 0 indicates the highest calculated uncertainty in phase velocity, and a value of 1 indicates the lowest calculated uncertainty in phase velocity.

2.4. Infrastructure

2.4.1. Justification Of Addition

Geothermal development faces significant restrictions across all of the Play-Fairway projects that bear directly on the feasibility of exploration, development, and operation of a geothermal project. Restrictions such as unfavorable zoning or land ownership, distance to transmission lines, proximity to seismically sensitive population centers, lack of process water, or adverse environmental factors can all cause a viable geothermal resource to be undevelopable.

2.4.2. Favorability Modeling

In order to focus validation activities in areas that are most likely to be developable, we constructed a state-wide infrastructure favorability model and clipped this model to our study areas. The model contains six data sets that reflect a comprehensive array of development factors and were combined into a final model using AHP.

Land ownership, leasing, and zoning restrictions:

> *Un-drillable land*—Washington contains many National Parks and Monuments, Wilderness areas, State Parks, and other lands upon which geothermal drilling and development is not allowed. These lands were identified and are used as an exclusion filter for the infrastructure model. Included in this category are some lands managed by the Columbia River Gorge Commission near the Wind River study area that are protected because of their value to the scenic Columbia River corridor.
>
> *Favorable land*—Three types of land were identified that have above-average favorability for geothermal development: (1) existing geothermal leases on private timber land, (2) existing or proposed geothermal leases on Forest Service land, and (3) state-owned (DNR) land for which geothermal leasing is available. Although development on private land outside of these identified areas is possible, in-place leases and leasing options represent a more streamlined path to development and permitting and ensure that industry and land managers have goal alignment.

Availability of process water: Geothermal power production can potentially consume significant quantities of water depending on reservoir characteristics and facility design, and water cooled power plants operate with much greater efficiency than those cooled by air in the summer months. Although most of our plays are located in temperate rainforest with annual rainfall of 2–3 m (study areas average 3.1, 2.9, and 2.3 m/yr from north to south), other locations might face location restrictions based on water availability. To approximate regions with potentially abundant versus potentially scarce water resources we combined the 2010 PRISM mean annual

precipitation data with proximity to perennial streams, rivers, and major bodies of water. This simple model does not account for water rights, environmental protection, or water loss from evapotranspiration, runoff, aquifer storage, or many other factors that will need to be assessed on a site-specific basis. Equal weight was given to each layer and the maximum and minimum scaling values are provided in Table 14.

Table 14. Intermediate weights for process-water favorability layers.

Indicator	Criteria	Value	Layer weight
Mean annual precipitation	0 m/yr ≥2 m/yr	0 1	0.50
Proximity to perennial stream, river, or body of fresh water	0 km ≥10 km	1 0	0.50

Proximity to viable transmission lines: Distances less than ~20 km are considered feasible by industry but adding transmission lines beyond this distance is likely to be a significant impediment to development of power-producing facilities.

Proximity to existing roads: During Phase 3 validation it will not be possible to build new roads due to permits and cost; thus we buffer all roads to a distance of 250 m to ensure that potential drill sites are sufficiently close to existing roads.

Distance from urban centers: Induced seismicity is a byproduct at many geothermal facilities (e.g. the Geysers geothermal field; Eberhart-Phillips and Oppenheimer, 1984) and such side-effects are increasingly not tolerated by large population centers (e.g. Basel Switzerland; Mignan and others, 2015). We use the 2010 Census-defined urban areas and buffer these regions to a distance of 15 km with a linear ramp to zero at 25 km.

Elevation restrictions: Washington faces significant snow load at high elevations that might hinder infrastructure development. We consider areas above 8,500 ft to be unfavorable and areas below 4,500 ft to be insensitive to this constraint.

2.4.3. Confidence Modeling

No confidence modeling was performed on these data.

3. Results Of New Data Collection

3.1. Mount Baker Study Area

New data collection results at Mount Baker are shown in Figure 3 and are discussed below.

3.1.1. Geologic And Geomorphic Mapping

Aims: Interpret recently flown lidar, specifically looking for evidence of active faults. Field-check and improve previous geologic mapping.

Data Collected: Lidar with 1-m resolution covering most of the study area was flown in late 2015 and delivered to DNR in July, 2016 as part of the USGS 3DEP program at no cost to this project. Lidar was interpreted and accessible lineaments were field checked. Geological mapping

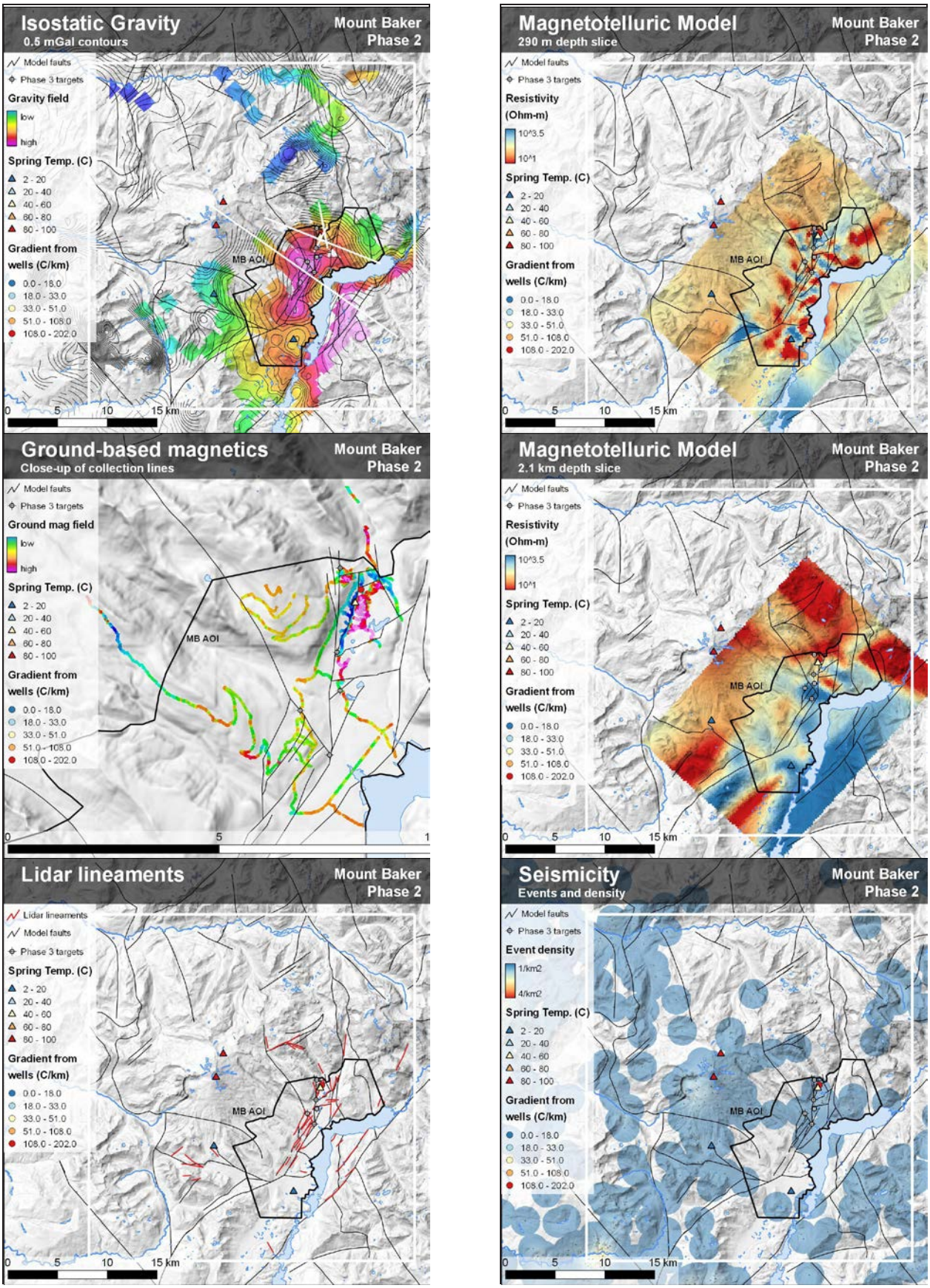

Figure 3. Newly collected data and existing seismicity at Mount Baker.

at 1:24,000-scale or better was conducted along and adjacent to lidar lineaments in the Area of Interest (AOI).

Major Findings: 57 linear features were identified from lidar and several are sub-parallel to or along strike from mapped faults; many lineaments also correspond to strong geophysical gradients and suggest that the geophysical boundaries are perhaps controlled by active faults.

Abundant fractures are found in exposures along these lineaments.

Existing maps are largely accurate at the 1:100,000-scale given the density of vegetation; some small updates were noted.

3.1.2. Magnetotelluric Survey

Aims: Determine 3D conductivity structure of study area to identify regions of enhanced fluid content, hydrothermal alteration, major structures, and geologic features.

Data Collected: MT data was collected using induction coils and electric dipoles at 28 stations throughout and adjacent to the AOI for a minimum of 20 hours per station. Data were processed and inverted to develop a 3D resistivity model from the surface to ~10 km depth.

Major Findings: A tabular 2–3 km^3 conductive zone was discovered from near the Baker Hot Springs to >3 km depth; this is also near a >200 °C/km temperature-gradient well (DNR 83-3). The conductive anomaly is similar in value to the measured resistivity of the hot spring water (~10 Ω-m) and is interpreted as a volume of upwelling hot fluid that perhaps ascends along a steeply north-dipping fault. The conductive zone nears the surface about 200 m east of the hot springs and moves west towards the springs along a surficial geologic boundary (perhaps glacial deposits).

The hot water discharging at the hot springs does not necessarily flow from beneath Mount Baker, but may be meteoric recharge that flows down along a S-dipping fault to 2–3 km before convecting upwards towards the hot spring.

Bulk porosity in the conductive anomaly near the hot springs may be 15% or higher.

There are many near-surface conductive anomalies; most are likely related to Quaternary glacial and (or) land-slide deposits.

Deeper conductive anomalies are found in areas where mapped faults intersect or where intersecting faults are interpreted from lidar and other geophysical data sets. This finding appears to support our conceptual model (Fig. 2) of enhanced permeability near geometric fault complexities that promote dilatant failure mechanisms.

3.1.3. Ground-based Gravity And Magnetic Surveys And Geophysical Modeling

Aims: Constrain subsurface geology and potential fault locations.

Data Collected: Over 93 km of magnetic data were collected using a backpack-mounted magnetometer and integrated GPS unit with a base-station magnetometer to correct for diurnal field

variation. Data were processed and inverted to develop a 3D subsurface model of magnetic regions in addition to map-view anomalies. This effort was undertaken as part of an outstanding undergraduate senior thesis at Western Washington University.

A total of 495 gravity observations were made in and near the AOI using a nearby base station to compute absolute gravity values and correct for instrument drift. These data were tied into regional gravity measurements through repeat surveys of older stations. Data were processed and used to develop an isostatic gravity map and identify the location of maximum horizontal gradients. Two cross sections were constructed and modeled with the potential field data to constrain the subsurface extension of mapped and inferred structures and provide cross-validation with other geophysical data such as seismicity, seismic tomography and MT.

Major Findings: 93 km of walked magnetic lines reveal a 1.7-km-long highly magnetic body along the lidar lineament that trends into the hot springs. The size and shape of the body was inversely modeled in 3D and was determined to be a roughly tabular, ~2 km^3 body that roots down to the NW near the conductive MT anomaly. The feature is consistent with being either a low-conductivity mafic intrusion—based on its geometry perhaps intruded along a fault zone—or an anomalously magnetic portion of the Permian metavolcanic bedrock—perhaps related to hydrothermal alteration. A steeply SE- or NW-dipping fault likely forms the NW boundary of this feature and corresponds to the strong magnetic gradient, lidar lineament, and location of the hot springs.

Magnetic data also reveal an intersecting steep NE-trending magnetic gradient ~0.5 km north of the hot springs. Interaction of the two structures may enhance permeability near the springs.

Both structures noted above have surface expressions in lidar and bound highly conductive regions in the MT model.

Many other steep magnetic gradients were identified, several of which lie along lidar lineaments and suggest recent deformation along these relatively large crustal structures.

495 new gravity stations significantly update and refine the existing isostatic gravity map of the area. Major density contrasts were identified using algorithmically determined maximum-horizontal gradient lineaments or ‘spots’ and large changes in the orientation of gravity contours. Many of these features correspond well with mapped faults and lidar lineaments.

Gravity and magnetic data were used to validate 3 geologic cross sections in the area via a forward-modeling process: a steeply SE-dipping fault is the simplest hypothesis that agrees with available observations.

3.1.4. Electrical Resistivity Survey

Aims: Check mapped faults and lidar lineaments for conductive anomalies indicative of fluid pathways or clay caps. Improve characterization of shallow fault geometry.

Data Collected: Two 355 m Electrical Resistivity (ER) transects were collected: one across a mapped fault and another across lidar lineaments. The IRIS Syscal R1 PLUS 72 electrode system was used to collect data with a dipole-dipole array and 5 m probe spacing. The data were pro-

cessed using Prosys RES2DINV software and corrected for topography. Detailed logs will be provided in the final technical report.

The ER method was not well-suited for this project for two main reasons: (1) the probes cannot get wet, a difficult feat in the temperate rainforest of Washington, and; (2) the probes must be in a 355-m-long straight line, also difficult in a temperate rainforest in steep terrain. Processed errors were extremely high (12–40%). Only one of six transects showed a change in resistivity across a known or suspected (lidar-based) fault. This was particularly frustrating because one of the transects (MSHSZ-ER1) crossed several well-exposed faults with abundant slickenlines and fault gouge, yet showed no correlation with changes in resistivity.

Major Findings: The MB-ER2 transect at Mount Baker is one of the only transects that showed a change in resistivity near a mapped lidar lineament; this transect also has the lowest error (12.7%). A 30-m-tall near-vertical resistivity contrast is found below a 10–20-m-thick conductive cap; the high conductivity zone may represent a clay cap or fluid filled fractures.

3.2. Mount St Helens Study Areas (North And SouthAOIs)

The results from new data collection at Mount St Helens are shown in Figures 4 and 5.

3.2.1. Geologic And Geomorphic Mapping

Aims: Map geology in northern AOI above the St. Helens Seismic Zone (SHSZ); specifically look for evidence of faulting, permeability pathways, potential heat sources, and hydrothermal alteration. In addition, lithological mapping provided information on the distribution of potential reservoir cap rock. Interpret newly acquired lidar.

Data Collected: Over 130 km^2 was mapped at 1:24,000-scale or better in the northern AOI, including more than 100 fault observations and 1,200 outcrop descriptions. The mapping partially overlaps and confirms the results of unpublished field notes and maps from Russ Evarts and Roger Ashley from the mid 1990's; we use their data to extend mapping coverage an additional 25 km^2 south beyond the Phase 2 mapping effort.

Major Findings: The surface expression of the NNW-trending SHSZ is an en echelon array of discontinuous lidar lineaments and newly mapped fault segments with argillic alteration. The soda spring in the northern AOI lies along one such newly mapped structure.

A diorite intrusion, mapped west of the SHSZ, appears to have altered and magnetized the surrounding country rock, is spatially associated with faults that are commonly silicified, bleached, sulfide-bearing, and often exhibit liesegang banding. This intrusion is late Eocene–early Oligocene (see Geochronology below) and is most likely the Spud Mountain pluton of Evarts and others (1987).

Faults with argillic alteration mostly strike ENE to ESE but also NW and likely record slip at relatively shallow crustal levels (<1–2 km). Faults with silicification, sulfides, and liesegang banding predominantly strike NNE to NE and likely record slip at deeper crustal levels (2–3 km); these faults are associated with the Spud Mountain pluton and may have been exhumed by regional eastward tilting (Evarts and others, 1987).

Faults of both argillic and silicic alteration have slickenlines that record paleo-stress similar to the modern stress field (~N-S σ1, horizontal compression), indicating that most faults in the area have the potential to still be active.

3.2.2. Geochronology

Aims: Determine age of newly mapped intrusive igneous rocks and previously mapped but un-dated rocks to assess their contribution to Quaternary geothermal heat potential.

Data Collected: Three intrusive igneous samples were dated by the OSU Argon Geochronology Lab using the $^{40}Ar/^{39}Ar$ method: one from the Spud Mountain pluton, one from a dike and sill complex that cuts the Spud Mountain pluton, and one from a series of basaltic dikes near Cold-water lake.

Major Findings: All three samples were latest Eocene to early Oligocene in age and document a previously unrecognized late Eocene period of plutonism.

3.2.3. Magnetotelluric Survey

Aims: Determine 3D conductivity structure of study area to identify regions of enhanced fluid content, major structures, and geologic features.

Data Collected: MT data were collected using induction coils and electric dipoles at 41 stations (northern AOI) and 15 stations (southern AOI) for a minimum of 20 hours per station. Data were processed and inverted to develop two 3D resistivity models from the surface to ~10 km depth. Both models incorporate constraints and boundary conditions imposed by nearby as-yet unpublished MT data collected for the iMUSH experiment.

Major Findings:

Northern AOI

A conductive column rises to just beneath the soda springs in the north part of the AOI and is the preferred drill target based on the resistivity model. The conductive column is ~10 Ω-m, which may indicate less fluid or perhaps greater mixing with meteoric water than the NNW-striking conductive anomaly just to the north (see below). Porosity is estimated at 2–10%; the estimate could be improved with conductivity measurements at the spring.

A 1-km-wide conductive zone (1–30 Ω-m) strikes NNW between 4 and 10 km depth. This conductive anomaly is coincident with and west of seismic events on the SHSZ. It is likely caused by either fluid-filled fractures or conducting phases such as graphite which could be present in Eocene-age organic-rich sediments that may underlie the exposed volcaniclastic rocks. Passive-seismic tomography indicates this zone highly attenuates shear waves (see below) and suggests that fluid-filled fractures are more likely than graphite. Porosity is estimated at 5–15% in this zone using a modified Archie's equation and assuming a water conductivity close to sea water (1 Ω-m).

A second drilling target may be a W-dipping column of high conductivity, but there is no surface manifestation of upwelling fluids.

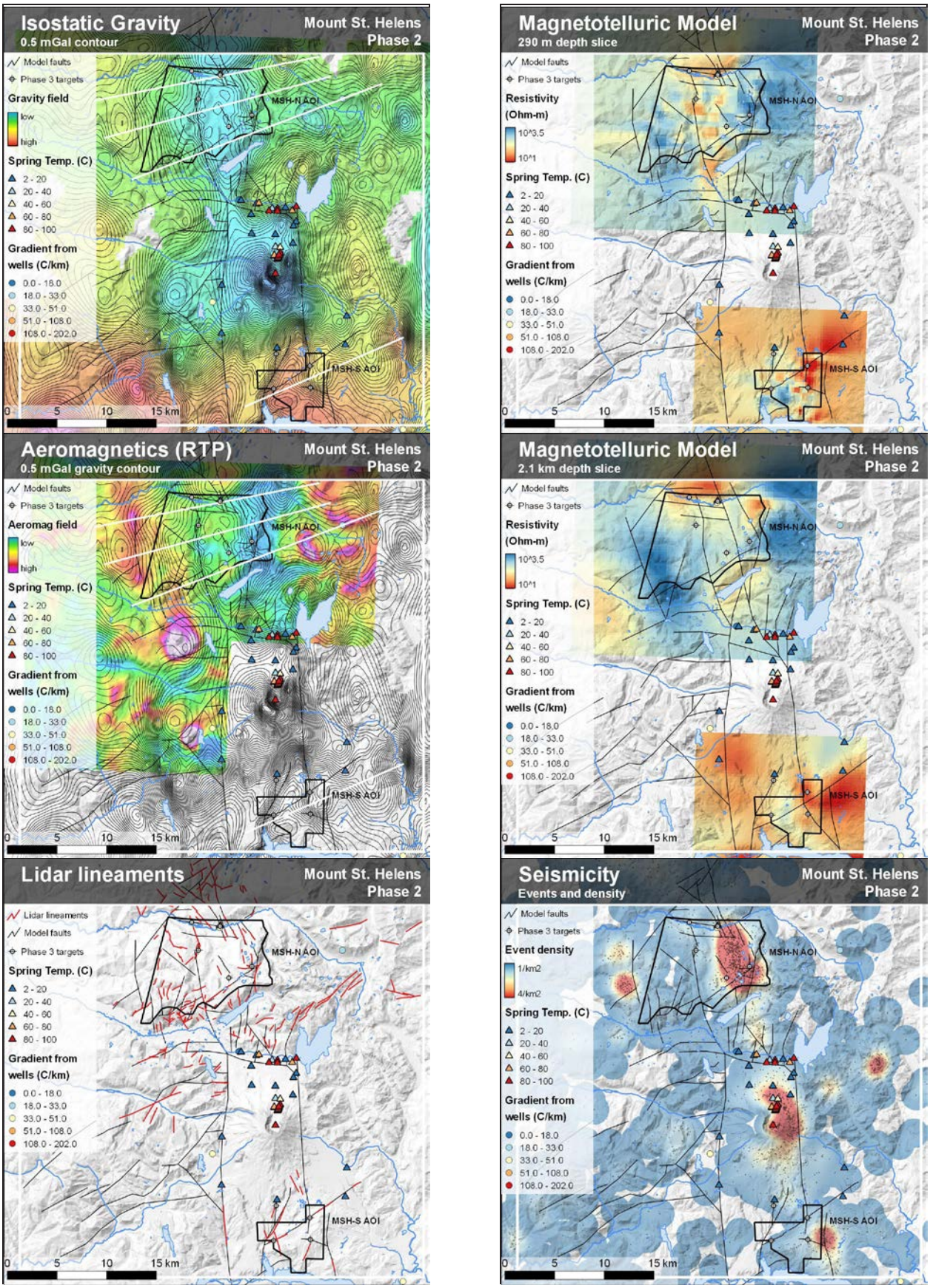

Figure 4. New gravity, MT, and lidar interpretation with existing seismicity and aeromagnetics at MSH.

Other near-surface features are the resistive blocks on either side of the SHSZ; the Spud Mountain pluton on the west and the Spirit Lake pluton on the east which help to define the overall crustal structure.

Southern AOI

The main feature is a 1-km-wide conductive (10–30 Ω-m) anomaly in the northeast that rises to near the surface; this is the preferred drilling target from the resistivity model. Similar to the northern AOI, the anomaly is adjacent to and above seismicity on the SHSZ. Assuming a lithology similar to the north, the lower zone of conductivity may have a lower fracture density—and thus lower fluid content—or mixes with fresh meteoric water. Porosity is estimated at 2–10% for the near surface conductive anomaly.

Seismicity is more scattered in this AOI and suggests a broader zone of weakness (and perhaps lower fracture density) than in the northern AOI.

A conductive block on the west of the AOI is most likely plutonic rock.

3.2.4. Ground-based Gravity Survey And Geophysical Modeling

Aims: Constrain subsurface geology and potential fault locations.

Data Collected: New gravity measurements were made in the northern (297) and southern (184) AOIs. Raw data were tied to an absolute datum and corrected for instrument drift through the use of a base station and were tied into regional gravity measurements through repeat surveys of older stations. Five new ground magnetic transects were walked with data collection and processing following procedures described at Mount Baker. Hand samples were collected for every major lithology and magnetic susceptibility, magnetic Q, and density values were measured. These data—along with a recently flown aeromagnetic survey—were used to model and match the potential field response along four cross sections.

Major Findings:

Northern AOI

The NNW-trending SHSZ is collocated with the western edge of the Spirit Lake pluton, which at this latitude is dense (~2,700 kg/m^3) and has a magnetic roof (60 x 10^{-3} SI, 0.17 A/M). Modeling confirms that this pluton extends from the upper crust perhaps into the mid-crust. Spatial variability in the potential fields along the modeled western edge of the pluton is mimicked by the pattern of microseismicity.

The western edge of the AOI contains the dense and magnetic Spud Mountain pluton (2,740 kg/m^3, 25 x 10^{-3} SI, 0.37 A/M). A suspected NNW-trending fault parallels the SHSZ—and coincides with the eastern edge of the Spud Mountain pluton—in the southern part of the AOI, but continues as a linear gravity gradient to the north as the edge of the pluton steps west. Thicker zones of Quaternary or late Tertiary cover are located between this fault and the SHSZ with the thickest sections close to each fault.

A zone of lower density nonmagnetic rocks (2,670 kg/m^3) forms a NNW-trending gravity low be-

tween the plutons and is consistent with lightly metamorphosed sedimentary rocks or more-felsic intrusive rocks. This lower-density nonmagnetic region encapsulates a highly conductive zone imaged with MT which is moderately to highly magnetic. A hypothesis of warm fluids circulating to shallow depths and precipitating magnetite is consistent with available potential-field observations. This hypothesis is also supported by observations that hornfels developed above the highly magnetic Spud Mountain pluton contain more magnetite than un-metasomatized rock.

Shallow warm fluids are most likely in the northern part of the AOI where the shallowest magnetic anomalies are found near the intersection of an E-trending structure and the SHSZ. A shallow conductive column in the MT model just east of the SHSZ is not magnetic and therefore we interpret this region as a zone of colder return flow instead of upwelling.

A gravity high bound by ENE-trending gradients along the Green River in the north of the AOI indicates a deeply seated cross-structure.

Southern AOI

A low-density (2,600 kg/m^3) and nonmagnetic region is collocated with a zone of high conductivity in the MT model and corresponds with the ~160 ka volcanic vents of Marble Mountain. This region is a gravity low between two more-dense (2,740 kg/m^3) and nonmagnetic regions interpreted as intrusive volcanic rocks. Cross sections are less-well constrained compared to the northern AOI because of fewer hand-sample measurements.

A narrow but dense and highly magnetic (2,700 kg/m^3, 30 x 10^{-3} SI, 1.12 A/M) zone is adjacent to the column of highest conductivity in the MT model and is interpreted as the basaltic feeder for the ~160 ka Marble Mountain basalts. Most of this feature is west of the vents. The surface vents are located above small-wavelength gravity lows that may represent buried scoria cones.

The strongest gravity gradients trend NE and E and appear to cross the NNW trend of sparse seismicity associated with the SHSZ.

As in the north, the most linear band of seismicity broadly marks the eastern edge of a lower-density region. This boundary appears to be the edge of a large upper to mid-crustal plutonic complex, similar to the Spirit Lake pluton. A strong NNW- to WNW-trending gravity gradient extends beyond the speculative pluton margin and marks the eastern and northern edge of a very strong gravity low containing the active Mount St. Helens volcanic edifice. Many mapped springs are coincident with this gravity gradient and may indicate that it blocks the northward flow of groundwater.

3.2.5. Passive Seismic Survey—Earthquake And Ambient-Noise Tomography

Aims: Define high-resolution subsurface velocity structure to aid in the interpretation of large-scale geologic boundaries, faults, and regions of fluid-filled fractures.

***Data Collected And Method Overview*:** A network of 20 broadband seismic stations were deployed from June through November of 2016 and combined with 70 stations from the iMUSH experiment (imush.org) and several permanent stations from the Pacific Northwest Seismic Network. Phase 2 seismic stations used Geotech KS2000M broadband seismometers with Reftek

130 and Smart24 data loggers, iMUSH stations used Guralp CMG-3T broadband seismometers and Reftek 130 data loggers, and PNSN stations are a mixture of short-period and broadband seismometers. The Phase 2 instruments had an array diameter of ~12 km and an average station spacing of 2 km; the iMUSH network has an average array diameter of ~100 km and station spacing of ~10 km.

Earthquake tomography data consisted of P- and S-wave arrival times from ~300 local earthquakes (~60 within the Phase 2 footprint, 40 of which occurred during the deployment). In total there were ~5,300 P-wave and ~2,500 S-wave arrivals which provided raypaths through the model volume, with 559 P-wave and 414 S-wave arrivals observed at Phase 2 stations. Earthquake P- and S- arrival times were picked using the seismic software package *Antelope*, and inverted to obtain 3-D seismic velocity models with the program *struct3dp*, written by Bob Crosson. This program uses a conjugate-gradient least-squares method with joint hypocenter and velocity inversion using 3-D eikonal-based travel time computation (Vidale, 1990; Hole and Zelt, 1995).

Ambient-noise tomography uses the cross-correlated continuous noise between seismic station pairs to provide a fundamental-mode Rayleigh-wave signal between the stations (Shapiro and Campillo, 2004). These cross correlations are then used to calculate velocities, which can be interpreted for structure. A new technique using radial-vertical cross correlations of ambient noise (Haney and others, 2012) was employed to image small features from a high-frequency dataset. This technique uses a frequency-domain method that calculates phase velocities and is well-suited for short (3 km-long) paths (Ekström and others, 2009, Jin and others, 2015) and thus high-resolution, shallow imaging. Finite-frequency tomography (Lin and others, 2009, Zhou and others, 2005) was also used which calculates the phase velocity tomography for small arrays more accurately than ray theory. Shear velocities are then calculated from phase velocities and are shown as depth slices in the model space where the resolution matrix for phase velocities is nonzero. This technique has been demonstrated in various hydrothermal and geothermal settings, such as Dixie Valley to develop EGS exploration methodology (Lovinetti and others, 2012) and Soda Lake as a cost effective alternative to active source seismic surveys (Tibuleac and others, 2012). Full documentation of the method will be available in the final Phase 2 report.

***Major Findings*:**

Earthquakes—There were approximately 20 events in the PNSN catalog within the Phase 2 array footprint during its deployment. These were relocated as a part of the seismic tomographic inversion, and 20 more were detected using the *Antelope* seismic software. Focal mechanisms were calculated for several of these. Earthquake focal mechanisms along the SHSZ are similar to previous results (Weaver and others, 1987), exhibiting right lateral shear, with T axes oriented in a NW-SE direction. Earthquakes ~15 km WSW of the SHSZ have T axes oriented closer to E-W.

Earthquake Tomography—Major features of the 3-D seismic velocity models include low P- and S-wave velocities along the SHSZ, possibly related to fluids or fractures. High velocities at shallow depths to the east and west of the SHSZ correspond to the Spirit Lake and Spud Mountain plutons. There are high Vp/Vs ratios just to the west of the SHSZ, which could indicate the presence of fluids, since S-waves are more sensitive to fluids and open fractures. Currently the P and

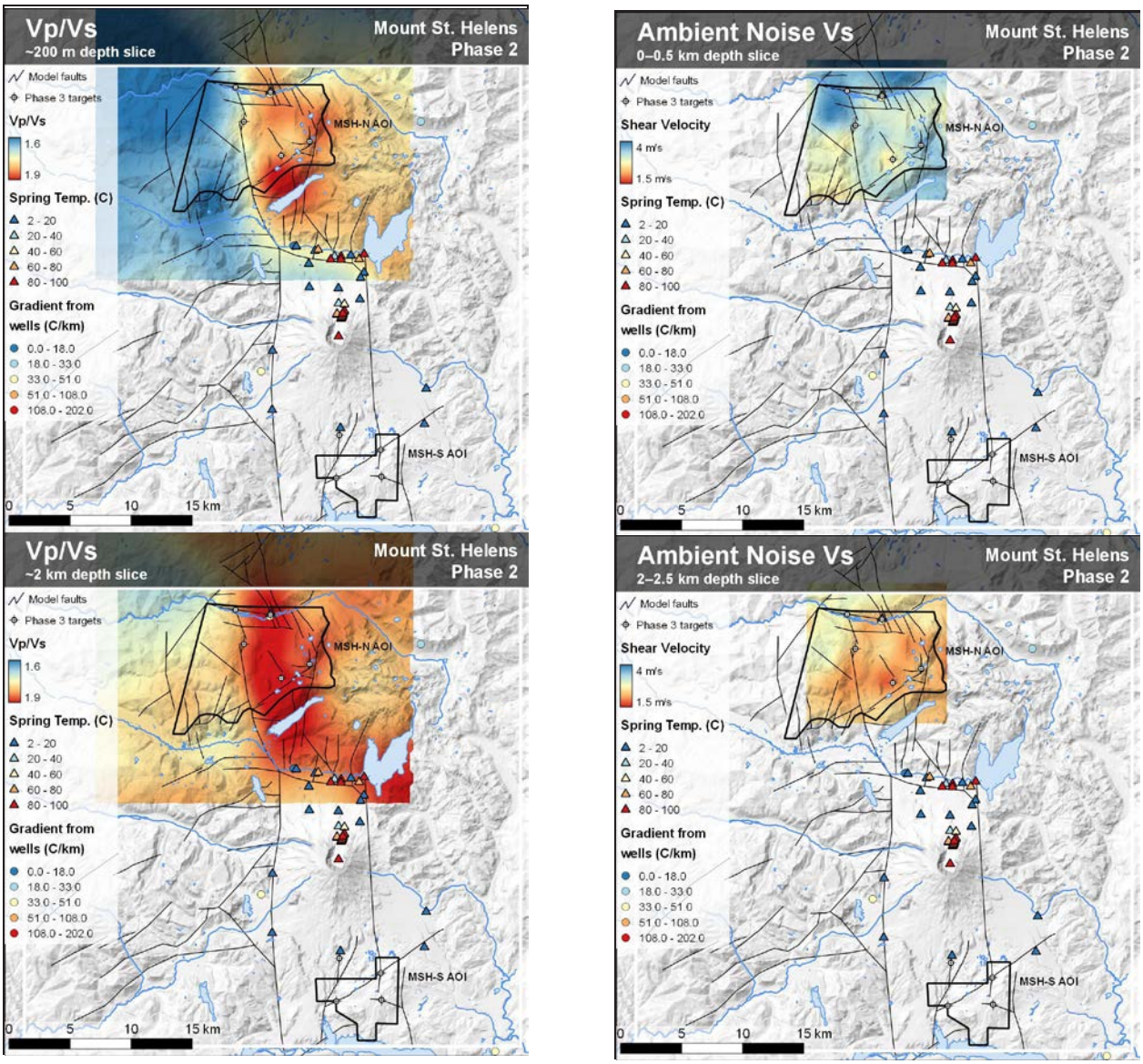

Figure 5. Results from passive-seismic studies at MSH.

S velocity models are inverted separately, but a simultaneous inversion to obtain the Vp/Vs ratio directly will provide a more robust result for the Vp/Vs ratio. This inversion is being performed as part of the iMUSH project and the results will be available this summer.

Ambient-noise Tomography—A central region of low velocity is identified and lies adjacent to the SHSZ (Fig. 5). The inferred fault of the SHSZ lies in an area of high velocity gradient; fast velocity is found to the E and slow velocity to the W and NW. The velocities farther W and NW (3–4 km/s) could be within the Spud Mountain pluton (Evarts and others, 1987); common shear velocities for diorite at 2–4 km depth are around 3.7–3.8 km/s. The fast velocities (2.2–3.6 km/s) to the E of the fault could be the edge of the Spirit Lake pluton, which should have a velocity near 3.6 km/s at 2–4 km depths. Near-surface porosity can lower the velocities of diorite or granite; however, the low velocities in the center of the map are much lower than the plutons (1.8–3 km/s) and indicates lower density or fractured rock.

3.2.6. Electrical-Resistivity Survey

Aims: Check mapped faults and lidar lineaments for resistive anomalies indicative of fluid pathways or clay caps. Improve characterization of shallow fault geometry.

Data Collected: Four resistivity transects were conducted at MSH following the same procedures as at MB. These transects also failed to respond to known faults with well-developed gouge and geomorphic expression. Because the method did not identify the well-exposed faults in the MSHSZ-ER1 transect, we have little confidence in the remaining sections. The results will be compiled in the final Phase 2 report but will not be discussed further here.

3.3. Wind River Valley Study Area

The results of new data collection at Wind River are shown in Figure 6.

3.3.1. Geomorphic Mapping

Aims: Interpret recently flown lidar, specifically looking for evidence of active faults.

Data Collected: Lidar with 1-m resolution was flown in late 2014, delivered to DNR in 2015 at no cost to this project, and interpreted using 1:24,000-scale mapping from 2014 to 'field-check' linear features.

Major Findings: 86 linear features were identified; approximately 40% corresponded to mapped faults, observed small shear zones, or areas of distributed deformation; approximately 30% correspond to linear alignments of maximum-horizontal gradients in the new gravity survey.

3.3.2. Geochronology

Aims: Determine age of plutonic rock proposed as a potential heat source for the Carson and Shipherd's hot springs.

Data Collected: A diorite sample from the Buck Mountain pluton was dated by the OSU Argon Geochronology Lab using the $^{40}Ar/^{39}Ar$ method.

Major Findings: A plateau age of ~20 Ma indicates there is a different source of heat for the hot springs. Currently, the most-likely candidate is the source of the abundant nearby late Pleistocene extrusive volcanism (Fleck and others, 2014).

3.3.3. Ground-based Gravity Survey

Aims: Constrain subsurface geology and potential fault locations.

Data Collected: 604 new gravity measurements were made and 4 new ground magnetic transects were collected. Data collection and processing followed the same procedure as MSH. These data—along with a previously flown aeromagnetic survey—were used to model and match the potential field response along three cross sections.

Major Findings: The location of the St. Martin Hot Springs (and source for the Carson Hot Spring Resort) coincides with the intersection between the Wind River fault and the Shipherds

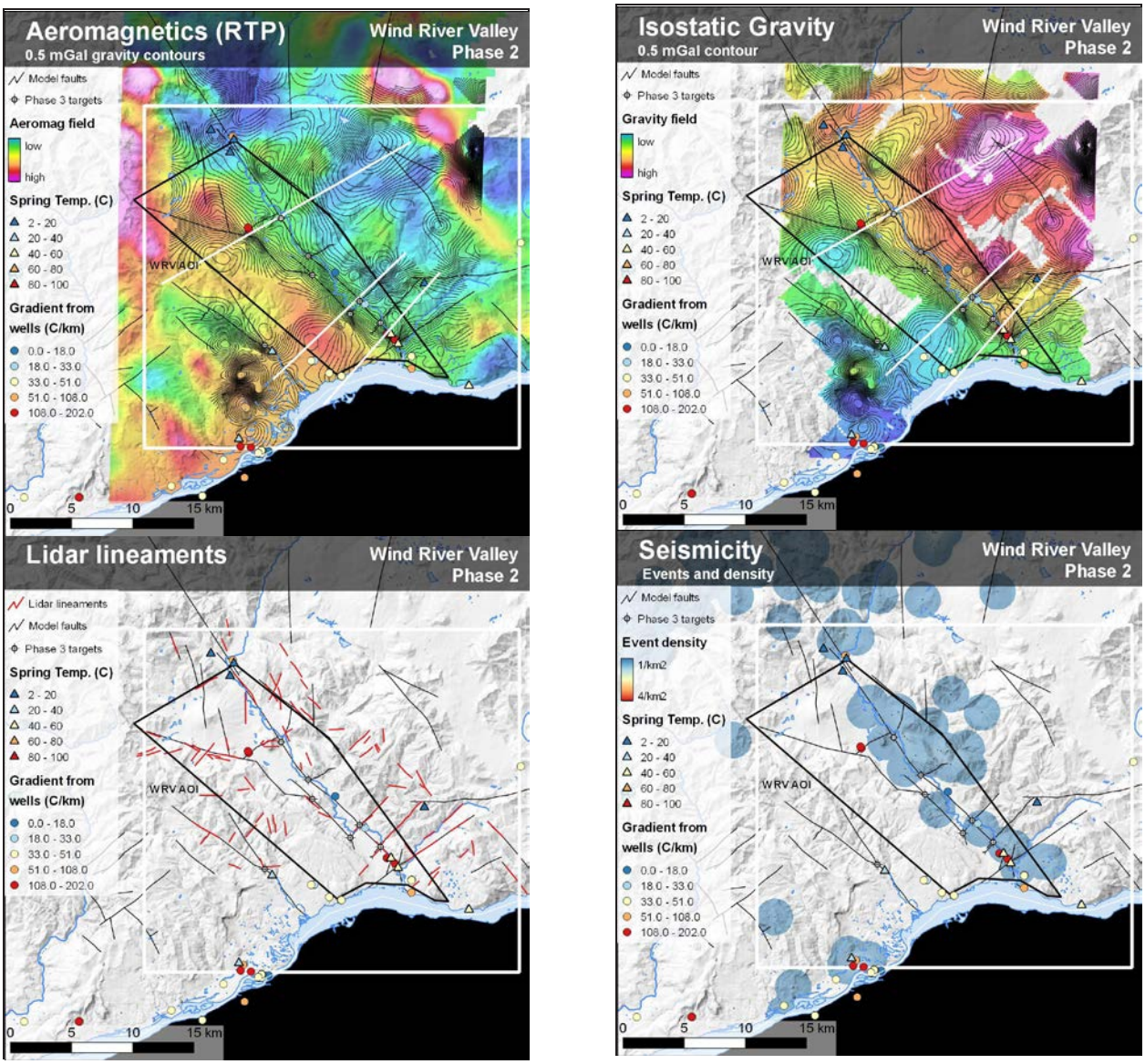

Figure 6. New gravity and lidar interpretation with existing seismicity and aeromagnetics at Wind River.

fault zone, which are well-defined in the potential fields by linear trends in maximum-horizontal gradient.

Gravity and magnetic data reveal a major crustal discontinuity running subparallel to the Wind River fault characterized by low density/high magnetization rocks on the SW and high density/ low magnetization rocks on the NE. A portion of the discontinuity is attributed to near-surface changes in lithology; the remainder require larger as-yet-unexplained changes at depth.

The Wind River Valley appears to be bound on both its NE and SW sides by subparallel structures. Complicated patterns of gradients in the NW part of the valley preclude the clear continuation of a through-going fault. The gravity and magnetic gradients on the SW side of the valley appear to trend farther WNW at the northern end of the valley.

The NE-striking Shipherd fault zone has a prominent geophysical signature and appears to mark

the SE boundary of a major crustal discontinuity. A steep gravity gradient continues NE from Carson Hot Springs, is subparallel to a mapped fault zone, and marks the transition between low density rocks on the SE and high density rocks on the NW. A parallel gradient is found in the aeromagnetic data.

The Brush Creek and Bear Creek faults are both observed in the isostatic gravity data, though the latter is less well defined. The Brush Creek fault is well defined by a sharp gradient subparallel to the mapped fault trace NNW of Buck Mountain. Though data are somewhat sparse to the east, this gradient then turns east and converges with the Shipherd fault zone.

3.4. Opportunistic Data Collection

3.4.1. Geochronology And Geologic Mapping

One regional study (Fleck and others, 2014) was completed since the last Washington statewide geochronology and volcanic vent compilation (Boschman and others, 2014) used in the Phase 1 heat model. This study collected over 100 $^{40}Ar/^{39}Ar$ ages which were added to our database and incorporated into our heat potential model. Additionally, two 7.5-minute quadrangles in the Wind River study area are nearing publication through the USGS and were provided to DNR by R. Evarts (USGS, written communication, 2016). Faults from these maps were added to the fault model, but fell outside of the smaller Phase 2 AOIs.

4. Updated Conceptual Models

4.1. Mount Baker Study Area

The updated conceptual model (Fig. 2) of the Mount Baker geothermal play remains speculative with regards to the pathway from the likely heat source (young intrusives or deeper magma below Mount Baker). Volcanic activity at Mt. Baker, most recently in 1975, can be responsible for extremely high heat flux below the volcano. Crider and others (2011) calculated that the heat-flux density in the crater increased from an already high 10 W/m^2 to 180 W/m^2 in 1975. This thermal increase could theoretically have been supplied by a sphere of magma 124 m in radius. Much better constrained by the new data is the structure(s) along which hot fluids upwell to the Baker Hot Springs and the nearby TGH with a measured gradient of 200 °C/km. Modelling based on ground-based gravity and magnetic data indicates that the structure trends south from the known upwelling locations, suggesting that a new temperature-gradient hole (TGH) drilled 1–2 km south would test this hypothesis, confirm the high heat flow previously measured, and provide an indication of the size of the geothermal resource.

4.2. Mount St. Helens Study Areas

The updated conceptual model (Fig. 2) is customized to the northern area of interest (AOI) and is consistent with the new data sets collected there. The seismically active SHSZ occupies a structural position between two plutons within a NNW-trending gravity low. The gravity low is consistent with lightly metamorphosed sedimentary rocks and are likely to be far weaker and more easily fractured than the adjacent intrusives. The abundant seismicity indicates that frac-

tures within the SHSZ are critically stressed. High Vp/Vs ratios and low MT resistivity suggest the presence of fluids (the geothermal reservoir) within the SHSZ. Within the lease area, this reservoir (between the plutons) could potentially measure 3–4 km E to W and 8 km N to S. Lastly, geologic mapping indicates that a thick sequence of altered volcaniclastics and volcanic flows are found between the plutons and comprise the reservoir cap. The primary uncertainty within the conceptual model is the heat source. The volcanic edifice of MSH is 15 km south and linked by the SHSZ; however, this distance is near the outer limit for vent proximity and geothermal prospects based on a study in Indonesia (Carranza and others, 2008, discussed further below).

4.3. Wind River Valley Study Area

The conceptual model of Wind River (Fig. 2) features two sets of major faults (NW striking and NE striking) which intersect at near right angles above a young, as-yet undiscovered heat source. The new data does confirm that the NE-trending Shipherd fault zone does have a prominent geophysical signature, although not as significant as the NW striking Wind River fault which largely controls the drainage and topography within the AOI. The existence of a shallow intrusion is still speculative yet seems required to explain the high heat flow indicated by multiple hot springs and temperature profiles from temperature-gradients holes.

5. Updated Phase 2 Favorability And Confidence Models

5.1. Definitions Of Terms Used

Assessment of geothermal systems is based on combining numerous data sets that each constrain a key element of the system. For each data set and resulting model we developed distinct metrics.

Favorability and potential—Both terms are used to refer to semi-quantitative assessments of data to develop a holistic geothermal model. In detail, favorability generally refers to the 0–1 value of a data set and potential generally refers to the weighted sum of several data sets.

Confidence vs uncertainty—Both terms refer to a semi-quantitative statement about the certainty of a value. Confidence is the direct complement of uncertainty and is used in Phase 2 instead of uncertainty. The phrase ‘confidence modeling’ refers to the assessment of certainty for both data-layer values and model results. Confidence as defined here then becomes a direct input into the assessment of risk.

Model risk—The term ‘risk’ is conceptually used here to refer to the likelihood of an outcome weighted by the certainty of the outcome. This is accomplished by scaling the favorability model by the confidence model; areas of high favorability with high model confidence are less risky than areas with high favorability but low model confidence.

5.2. Heat Potential

5.2.1. Phase 2 Activities And Model Additions

- Geochronology (MSH and WRV)
- Geologic mapping (MSH; opportunistic at WRV and MB)
- Revised model method

5.2.2. Phase 2 Results and Changes From Phase 1

The improved modeling method better defines regions of higher heat potential than the Phase 1 method. The Mount Baker area has the highest favorability of all three areas (Fig. 7), driven largely by the proximity of the Mount Baker volcano, Mount Kulshan Caldera, the young Lake Anne intrusive rock, several other young volcanic cones, and a 200° C/km temperature-gradient well. Favorability at Mount St. Helens is generally associated with the volcanic edifice with slightly elevated values in the southern AOI associated with the ~160 ka Marble Mountain volcanic vents and flows. At Wind River Valley, favorability is more-broadly distributed and is strongly influenced by the many temperature-gradient wells and abundant—but small—young volcanic vents. Weights for the input layers are provided in Table 15.

Although Phase 2 geochronology and geologic mapping did not identify young intrusive rocks capable of providing a geothermal heat source, the data from Fleck and others (2014) significantly improved the ages of young volcanic rocks in the Wind River area. The addition of new mapping and age control improved model confidence at MSH and WRV (Fig. 8).

5.3. Permeability Potential

5.3.1. Phase 2 Activities And Model Additions

- Geologic mapping (MSH, opportunistic at WRV and MB)
- Lidar interpretation (all areas)
- Detailed gravity surveys (all areas)
- Ground-based magnetic surveys (MB)
- Electrical resistivity surveys (new data at MSH-N and MB, previously collected at WRV)
- Aeromagnetic surveys (all areas; existing data, newly incorporated)
- 2D geophysical cross section modeling (all areas)
- 3D magnetic susceptibility modeling (MB)
- Refined boundary-element modeling of stress/strain
- Expanded fault slip and dilation tendency modeling
- Addition of seismic event density layer
- Addition of fault density layer
- Revised model method

Table 15. Summary of heat model layers, extents, and weights.

Input data layer	Brief description	Spatial domain	Avail-ability	AHP weight
Subsurface temperature observations	Temperature-gradient wells and wells with a bottom-hole temperature; weighted by quality	Study area	All	0.304
Springs	All springs with a measured water temperature	Study area	All	0.229
Quaternary volcanic vents	Proximity to vents; distance and weight vary by vent type and age	Study area	All	0.201
Quaternary intrusive rocks	Proximity to young intrusive rock; weight varies by age	Study area	All	0.139
Geothermometry	Estimates of reservoir temperature; weighted by quality	Study area	All	0.128

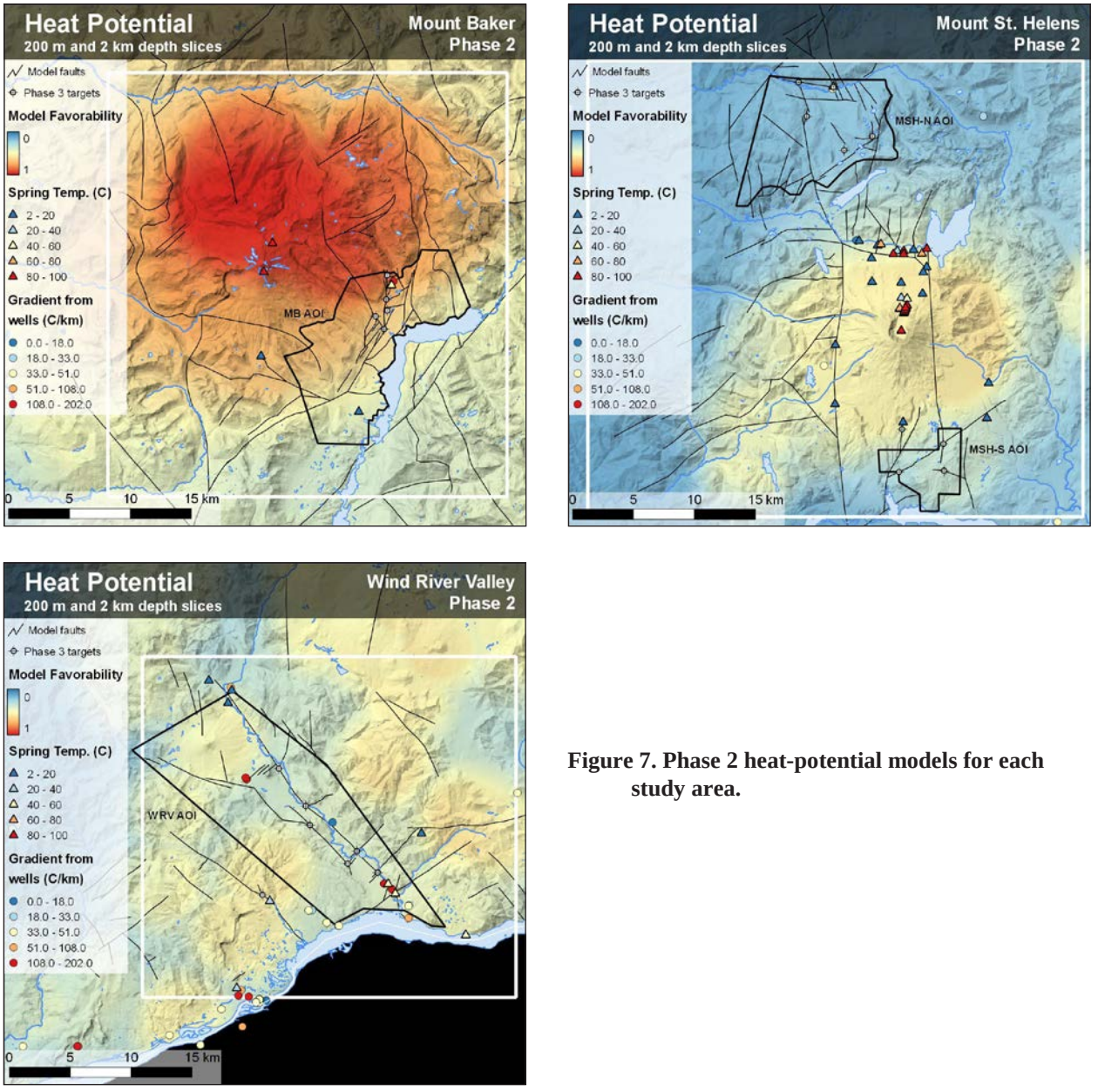

Figure 7. Phase 2 heat-potential models for each study area.

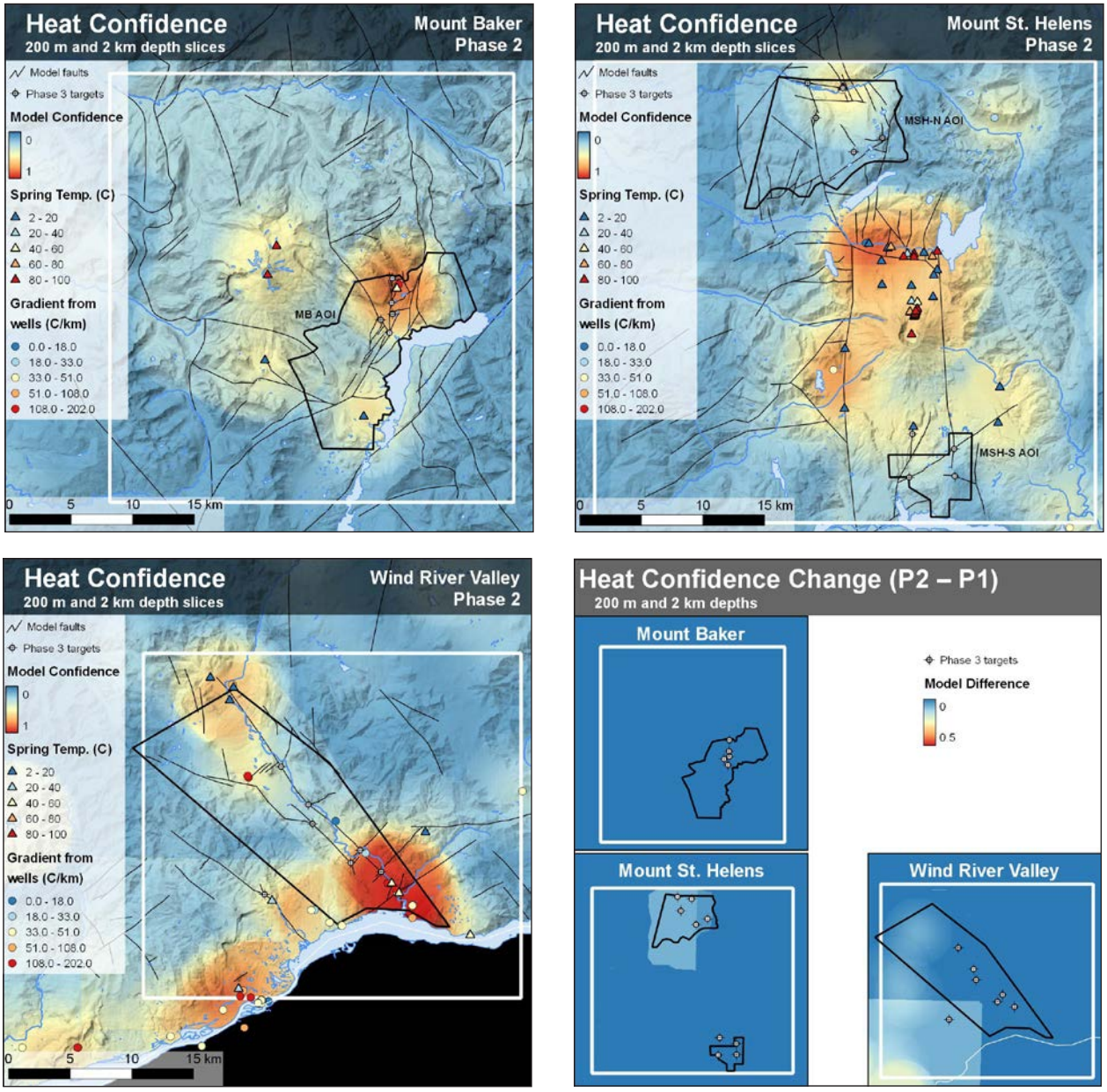

Figure 8. Phase 2 heat confidence models for each study area and change in confidence from Phase 1. Confidence increases are largely the result of new mapping at MSH, and opportunisitic data collection near WRV.

5.3.2. Phase 2 Results And Changes From Phase 1

Updating the permeability potential model (Figs. 9 and 10) was a focus of Phase 2 activities (Table 16) and shows the largest gains in model confidence. As in Phase 1, the most-favorable regions are located in areas of fault complexity (intersections, bends, and stepovers) where modeling suggests dilatant fracturing should occur under current stress conditions and where seismicity indicates deformation is occurring. In all study areas warm and hot springs are commonly associated with higher-favorability regions in the 200 m model, providing some independent verification of our basic modeling strategy. Notable exceptions to this are hot springs on the flanks of modern volcanoes which are more likely driven by very high heat flow instead of convective circulation through fracture networks.

5.4. Fluid-Filled Fractures

5.4.1. Phase 2 Activities And Model Additions

- Magnetotelluric surveys (MSH and MB)
- Passive-seismic Vp, Vs, and Vp/Vs tomography (MSH-N only)
- Ambient-noise shear-wave tomography (MSH-N only)

5.4.2. Phase 2 Results

This model is a new addition over Phase 1 and highlights regions that are most likely to have fluid-filled fractures (Figs. 11 and 12). Since data availability is vastly different between sites (Table 17), the AHP was conducted on a site-by-site basis and thus comparison of the resulting models should be done with care. In addition, most of these data sets have non-unique relationships to fluid saturation and temperature; the best results are achieved where multiple lines of evidence are integrated.

At MSH-N, where the most data are available, there is a favorable NNW-trending region that lies slightly west of and above the inferred fault defined by the SHSZ. This zone is high in conductivity, has a high Vp/Vs ratio, has slow ambient-noise shear wave velocity, and coincides with a gravitational low. Together, the collocation of these anomalies provide strong support for the presence of fluid-filled fractures; the soda springs in the north of the AOI lies along this trend at an intersection of favorable structures. Lower-favorability regions to the west and east correspond to the Spud Mountain and Spirit Lake plutons mapped at the surface and indicated in the sub-subsurface by higher seismic velocities, gravity anomalies and resistivity. In the southern AOI, a collocation of seismicity and a highly conductive anomaly in a high-amplitude gravity low provides compelling evidence for fluid-filled fractures.

At Mount Baker, high favorability is largely a product of high-conductivity MT anomalies; there is a small amount of seismicity in the NW part of the AOI near the hot springs. As discussed in Results of New Data Collection, a high-conductivity zone just north of the hot springs is interpreted as a region of fluid-filled fractures that provides a convective pathway from beyond ~3 km depth towards the surface; fluid from this anomaly likely mixes with cold meteoric waters in the last several hundred m before reaching the hot springs.

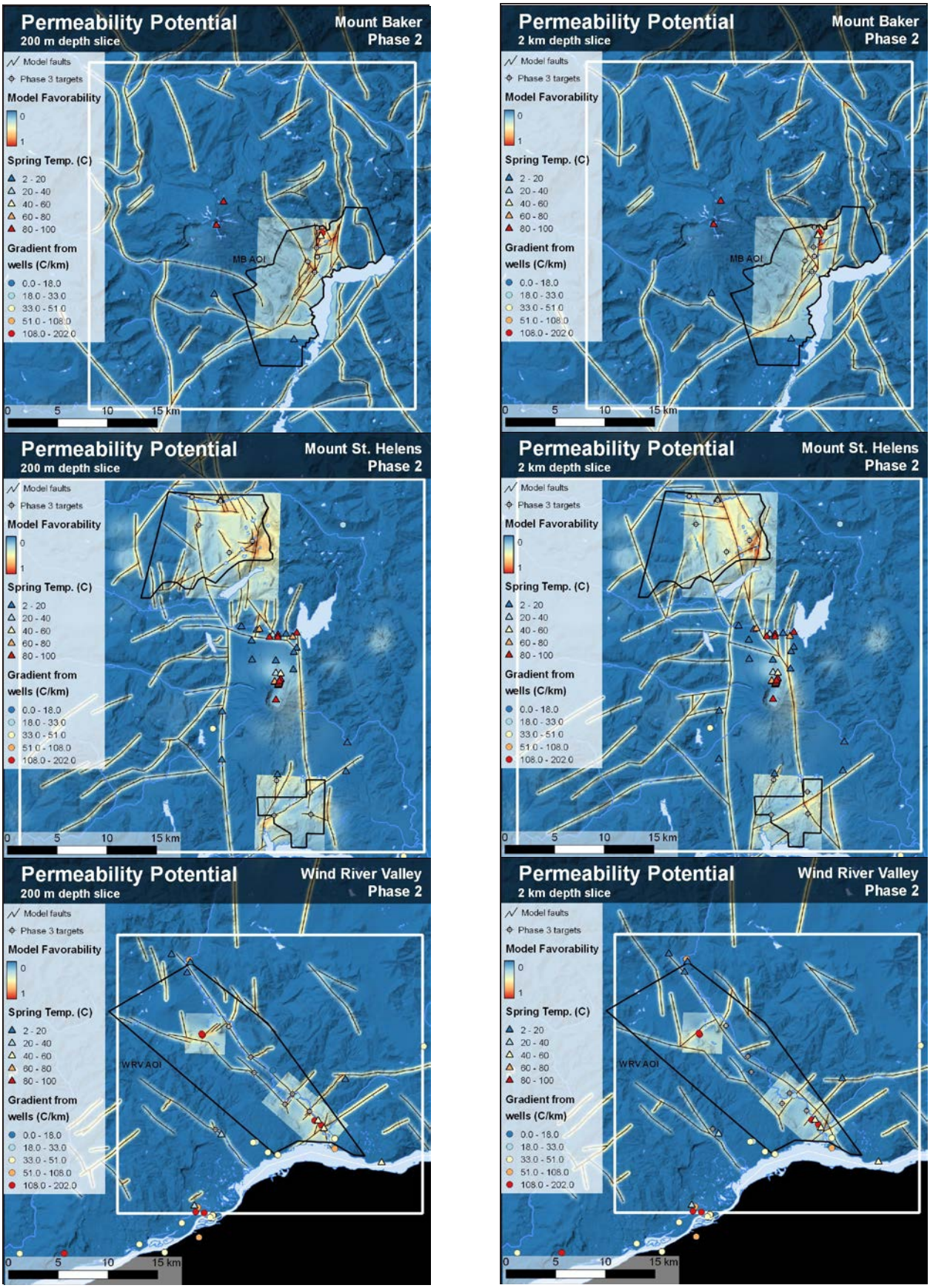

Figure 9. Phase 2 permeability potential models at 200 m and 2 km depths.

Table 16. Summary of permeability model layers, extents, and weights.

Input data layer	Brief description	Spatial domain	Availability	AHP weight
Fault density	Defines areas where faults are closely spaced or intersecting	Study area	All	0.330
Max. Coulomb shear stress	Defines regions where elevated shear stress (and fracturing) are likely	AOI	All	0.187
Dilation tendency	Defines faults and regions where dilational strain is likely	AOI and study area	All	0.142
Seismic-event density	Defines map-view regions of seismicity; provides inference of active deformation	Study area	All	0.138
Slip tendency	Defines fault segments likely to slip under current stress conditions	AOI and study area	All	0.113
Slip gradient	Defines regions along faults where fracture density is high due to complex fault geometry (e.g. fault tips, intersections and accommodation zones)	AOI	All	0.091

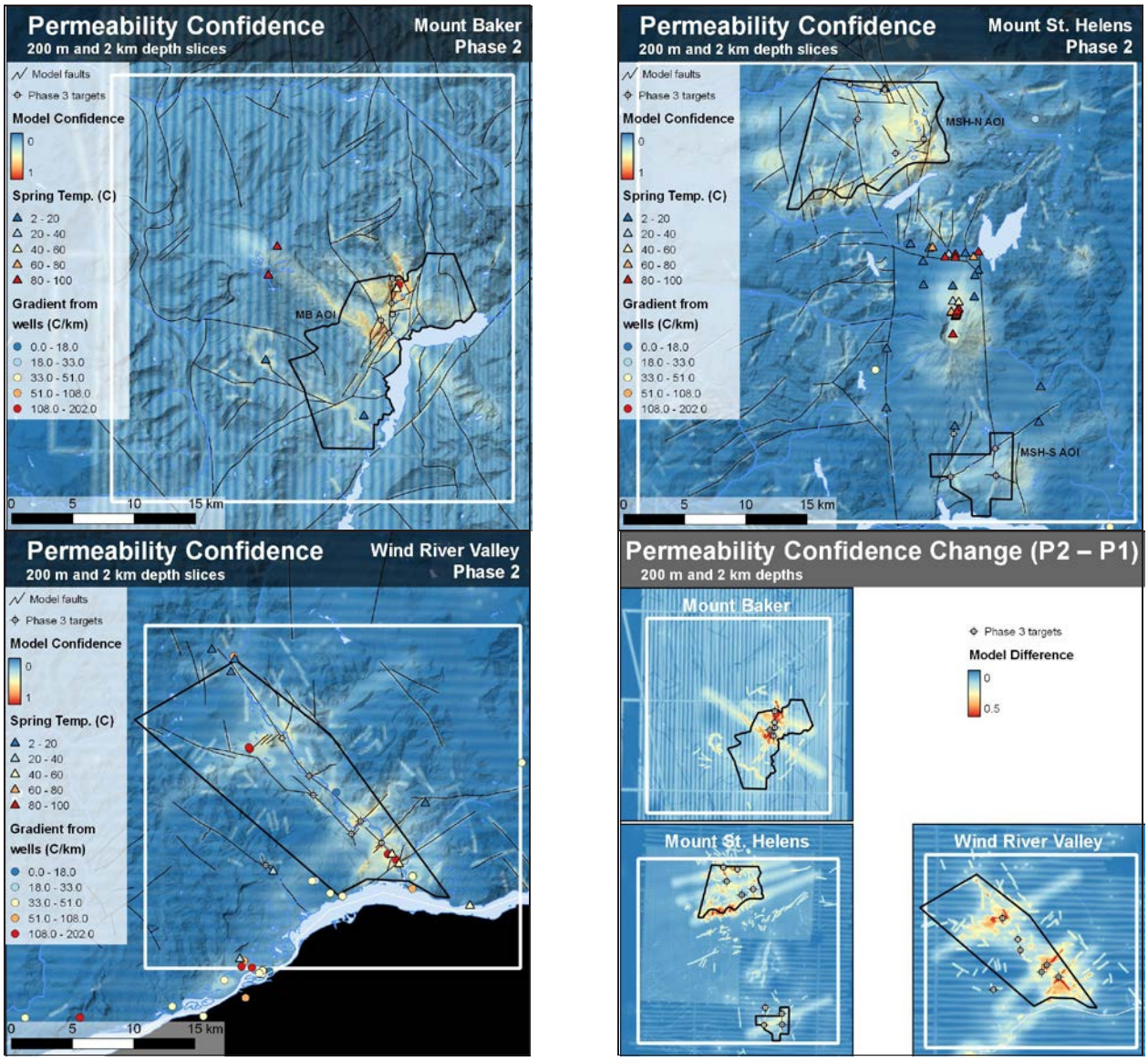

Figure 10. Phase 2 permeability confidence models for each study area and change in confidence from Phase 1 Confidence increases are the result of new mapping, lidar interpretation, the inclusion of new gravity and magnetic data, modeled cross sections, updated and refined geomechanical models, and opportunisitic data collection near WRV.

Table 17. Summary of fluid-filled fracture model layers, extents, and weights.

Input data layer	Brief description	Spatial domain	Availability	AHP weight (MB/MSHN/MSHS/WRV)
MT resistivity	High conductivity is interpreted as a region of fluid-filled fractures or conductive material	model area	MB, MSHN	0.318/0.587/– – –/– – –
Vp/Vs	High ratios indicate fluid-filled fractures are likely	model area	MSHN	– – –/0.310/– – –/– – –
Vs (ambient noise)	Areas of low shear velocity can indicate high temperature, high fluid porosity, and (or) rock composition.	model area	MSHN	– – –/0.148/– – –/– – –
Seismic-event density	Defines map-view regions of seismicity; provides inference of active fracturing	Study area	All	0.224/0.413/0.224/1.0

At Wind River Valley, evidence for fluid-filled fractures at depth is not well captured by the model because only seismic-event density was available. Flowing hot, warm, and cold springs throughout the region and abundant fault and fracture observations along the Wind River—many with small seeps or springs—provides some surface manifestations of fluid-filled fractures at depth. The presence of some seismicity along a NW trend parallel to the Wind River fault suggests active fracturing of rock at depth.

5.5. Combined Geothermal Model And Exploration 'Risk'

The three main models (heat, permeability, and fluid-filled fractures) were combined into two final models (at 200 m and 2 km depths) for each area that highlights regions with co-located high favorability (Figs. 13 and 14). Because of differences in data availability, weights were determined individually—using AHP—for each study area (Table 18). This strategy allows favorability values to be compared somewhat equally across all of the study areas; that is, MSH-N is not more favorable than WRV simply because it has more data. Confidence values were combined in a similar way; MSH-N generally has higher confidence than WRV, reflecting the value of integrating multiple independent lines of evidence.

Table 18. Summary of final model weights.

Model	MB	MSH-N	MSH-S	WRV
Heat	0.322	0.243	0.322	0.492
Permeability	0.344	0.351	0.344	0.388
Fluid-filled fractures	0.334	0.405	0.334	0.120

An exploration 'risk' model was developed for each study area and depth that scales the favorability by the confidence values (Figs. 15 and 16). Areas with low confidence have reduced favorability compared with high-confidence areas. It is noteworthy that low measured temperature gradients are found largely in areas of low favorability and the highest temperature gradients (in WRV and MB) are found in areas with the highest favorability (Fig. 15).

The scaled-favorability values were compiled for all existing temperature-gradient measurements in the study areas as a simple way to calibrate the model results. Although this approach lacks the independence (and high number of data points) of a true training/calibration study, autocorrelation between temperature-gradient measurements and the final model results is low because these data only contribute 4–7% towards the final model. A moderate positive correlation ($p=0.001$; $R^2=0.46$) is found when temperature gradient is regressed against confidence-scaled favorability; however, the lack of data near the center of the regression makes such an inference tentative.

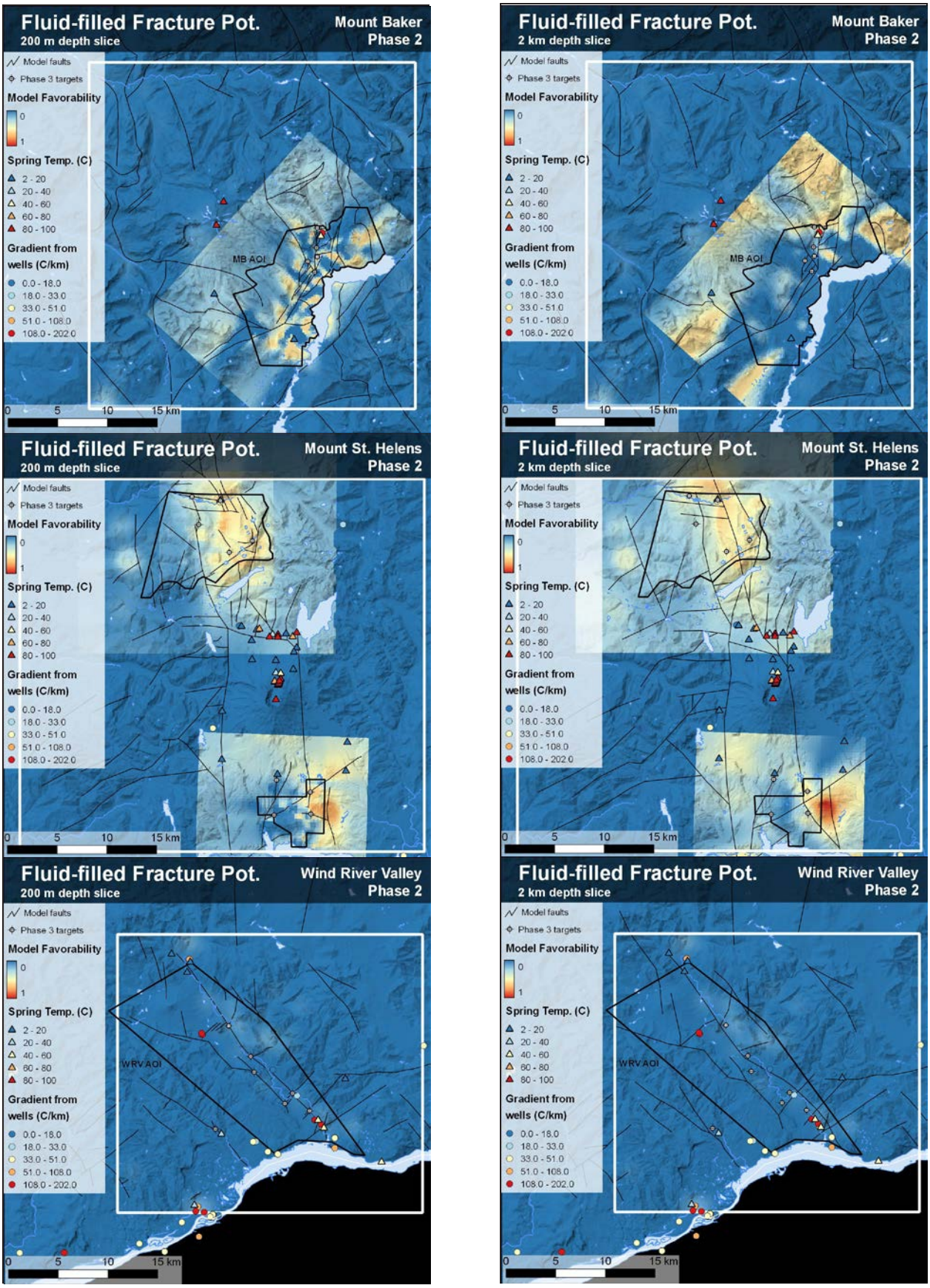

Figure 11. Phase 2 fluid-filled fracture potential models at 200 m and 2 km depths.

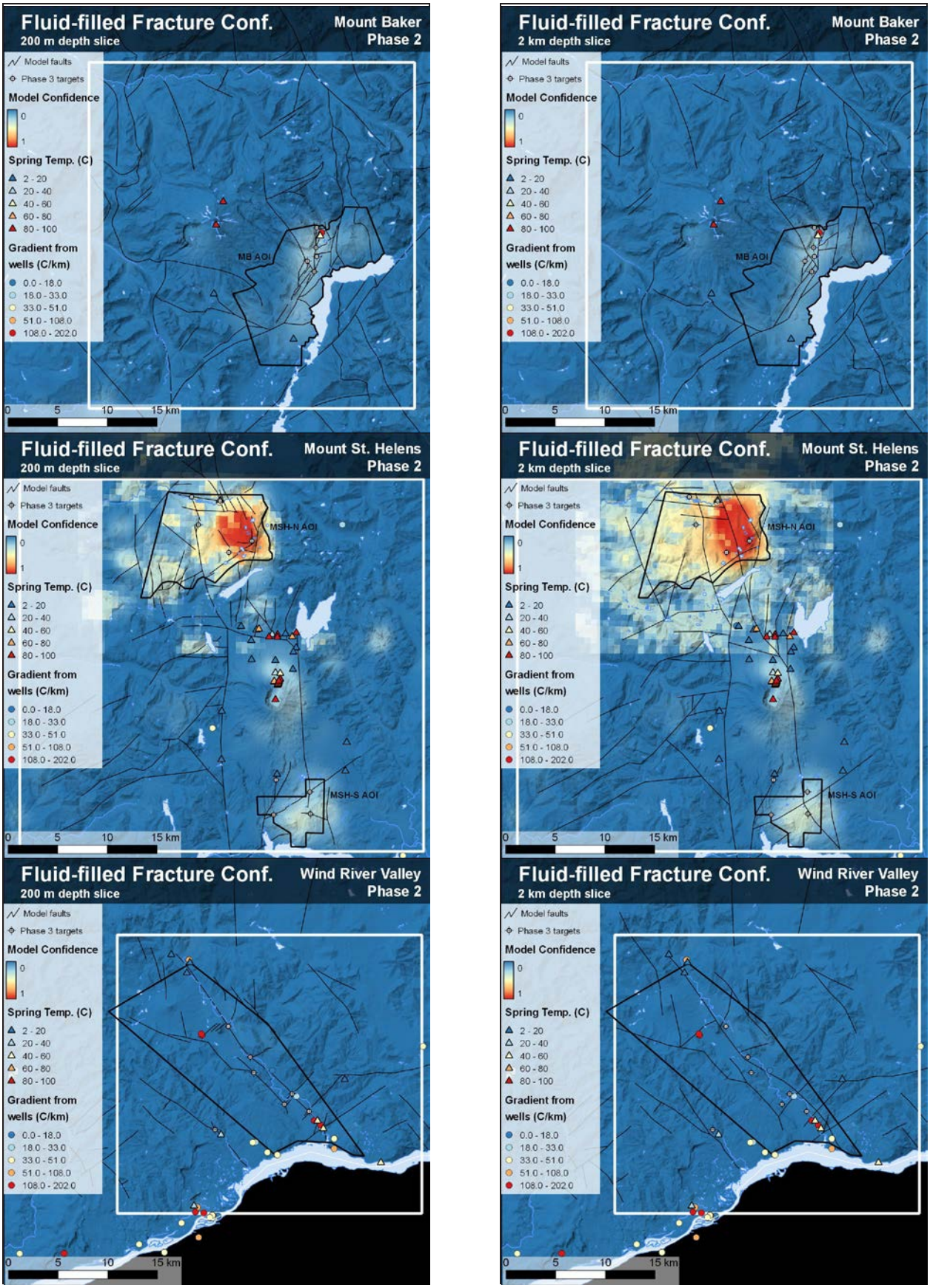

Figure 12. Phase 2 fluid-filled fracture confidence models. Data sets vary substantially between study areas.

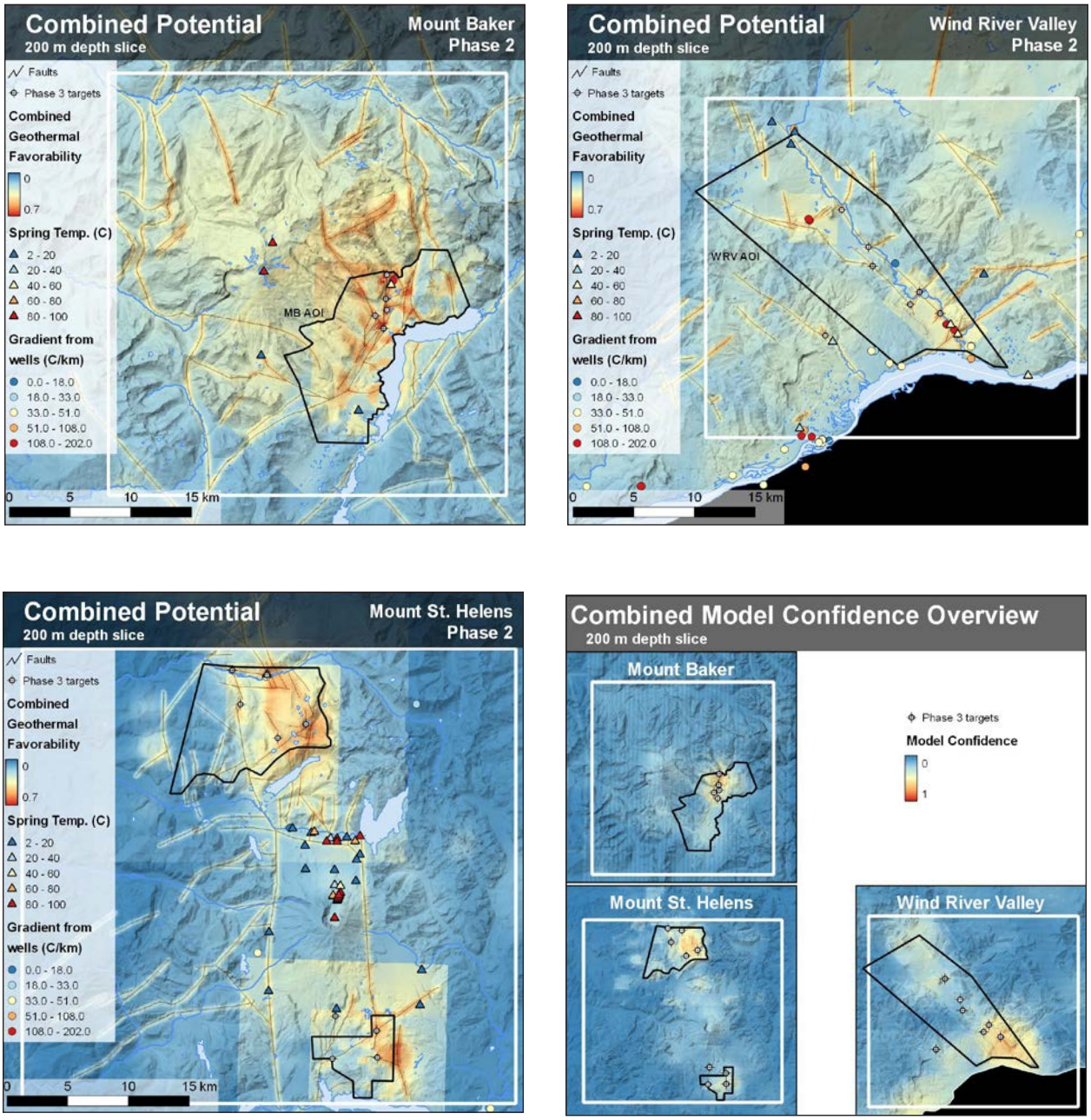

Figure 13. Phase 2 combined-favorability models at 200 m depth and overview of model confidence.

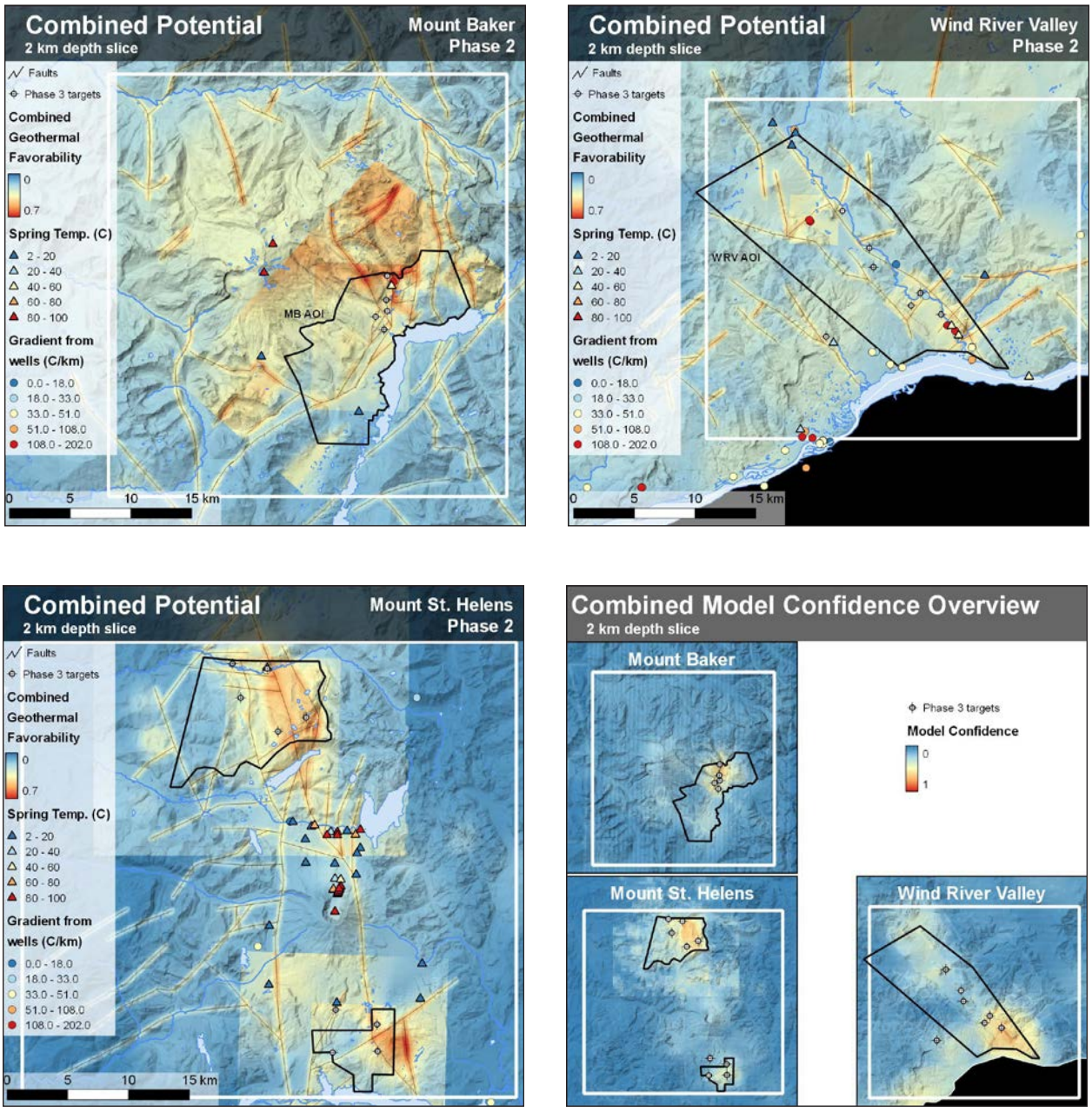

Figure 14. Phase 2 combined-favorability models at 2 km depth and overview of model confidence.

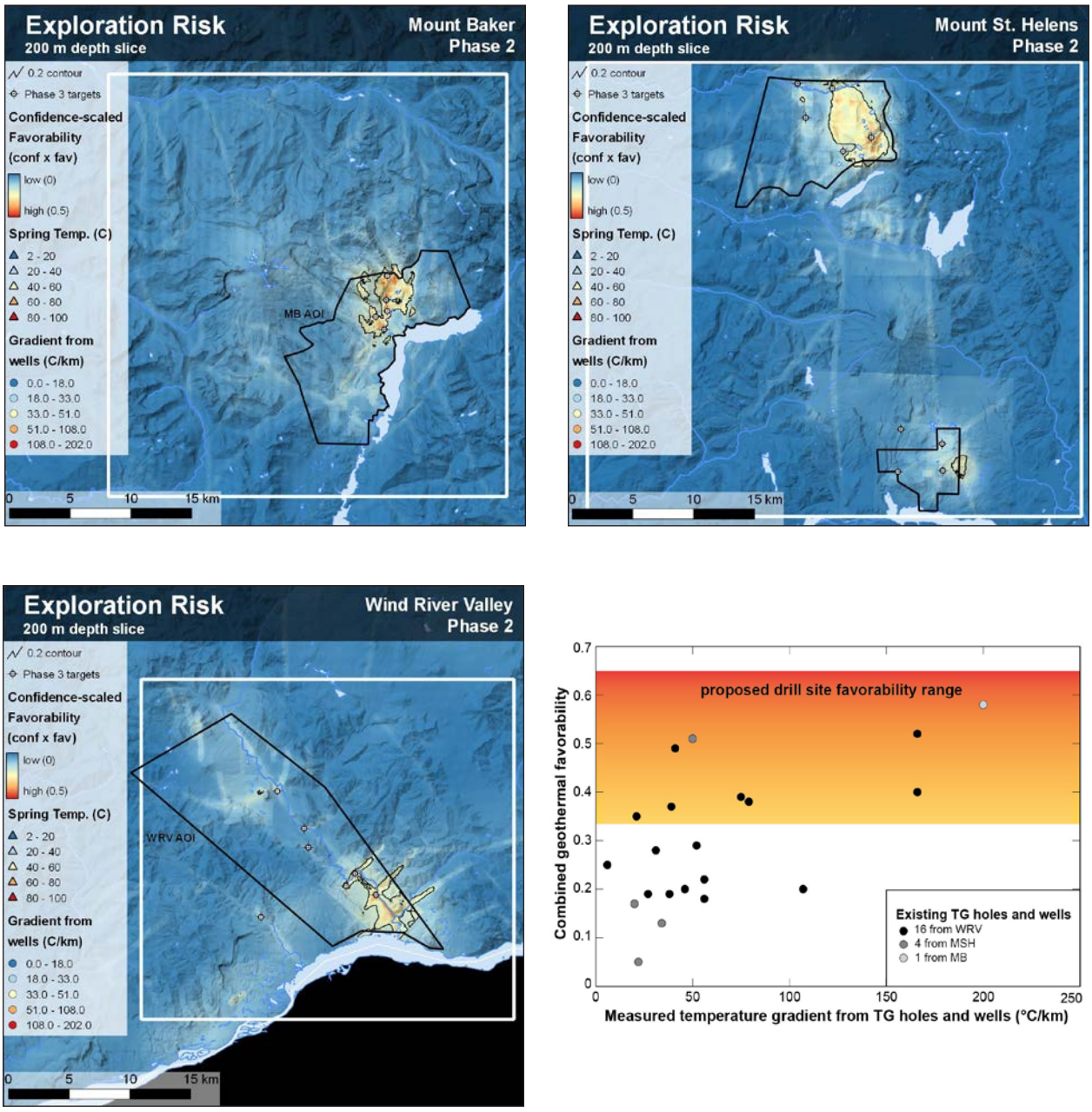

Figure 15. Exploration 'risk' models (confidence-weighted favorability) for all three study areas at 200 m depth and correlation between measured temperature gradients and model favorability.

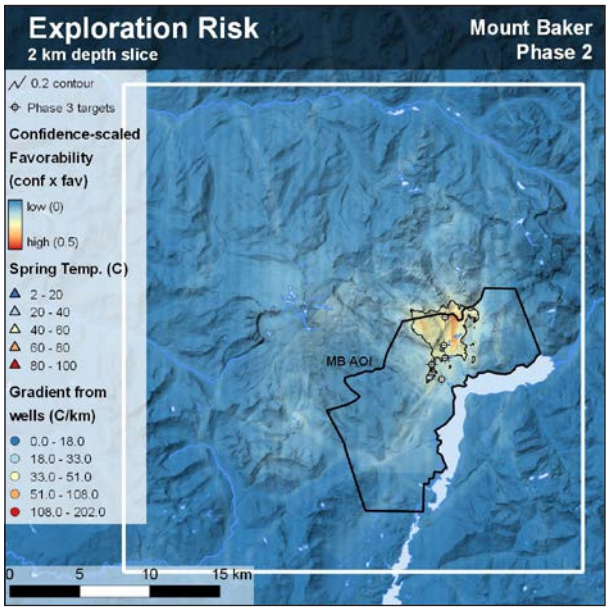

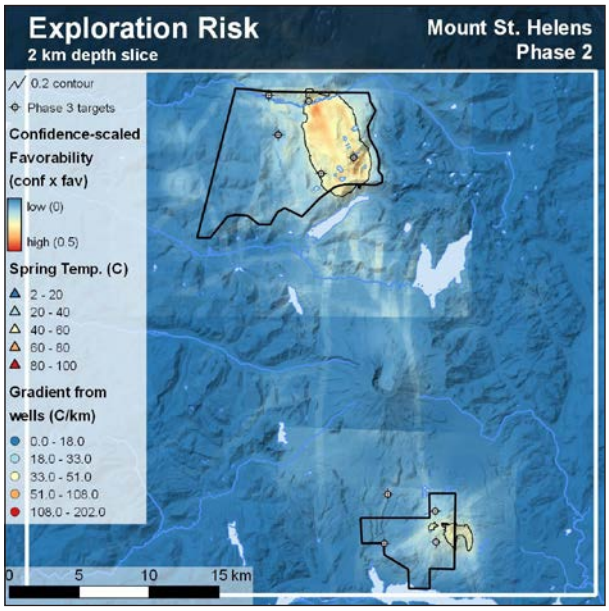

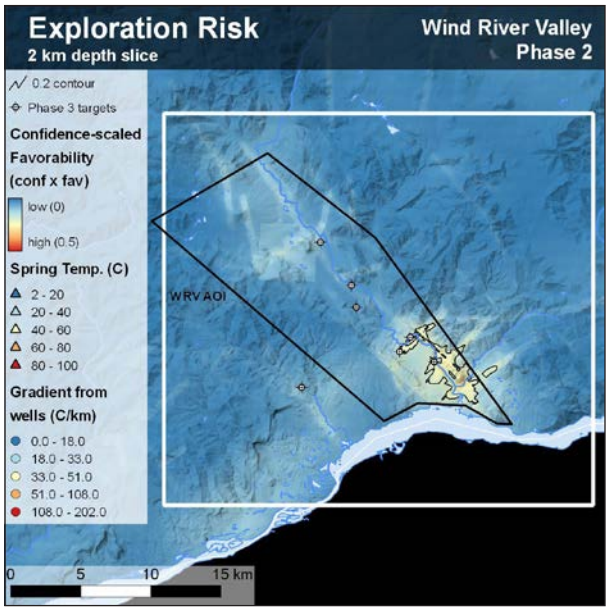

Figure 16. Exploration 'risk' models (confidence-weighted favorability) for all three study areas at 2 km depth.

5.6. Infrastructure

The infrastructure model formalizes many of the known constraints on the ability to successfully site, permit, and drill wells for a geothermal power plant. Model parameters and strategy are discussed in greater detail in the Revised and New Modeling Methods section. Model inputs are briefly described in Table 19.

The results of this model clearly show areas that are off-limits to drilling and highlight the favorability of the Phase 2 AOIs (Fig. 17). National Parks, Monuments, and Wilderness areas were the biggest off-limits areas; DNR-owned land and existing geothermal leases were the most-extensive favorable areas. Land-use restrictions along the Columbia River Gorge are substantial and were accounted for in this model. All of the areas are generally close to transmission lines; roads in Mount Baker were somewhat restricting. All of the areas were located at significant distance from major urban centers, and high elevations were not a significant limiting factor. Process water was non-restrictive, with 2–3 m/yr precipitation and abundant streams and lakes.

Table 19. Summary of infrastructure model layers, extents, and weights.

Input data layer	Brief description	Spatial domain	Availability	AHP weight
Land-use restrictions and favorable areas	DNR-owned land and existing or proposed geothermal leases; off-limits area mask the final model	Study area	All	0.243
Availability of process water	Mean annual precipitation and proximity to perennial streams and lakes	Study area	All	0.218
Proximity to viable transmission lines	<20 km buffer around 115 kV or greater lines	Study area	All	0.189
Proximity to existing roads	<250 m from existing roads	Study area	All	0.171
Distance from urban centers	>15 km from census-defined urban centers; accounts for societal effects of induced seismicity	Study area	All	0.101
Elevation restrictions	Increasing restriction above 4,500’ due to snow	Study area	All	0.077

REFERENCES

Boschmann, D.E., Czajkowski, J.L., and Bowman, J.D. “Geothermal favorability model of Washington State.” *Washington Division of Geology and Earth Resources,* Open File Report 2014-02, (2014), 20 p.

Bucknam, R.C., Hemphill-Haley, E., and Leopold, E.B. “Abrupt uplift within the past 1700 years at southern Puget Sound, Washington.” *Science*, v. 258, no. 5088, (1992), p. 1611-1614.

Carranza, E.J.M., Wibowo, H., Barritt, S.D., and Sumintadireja, P. “Spatial data analysis and integration for regional-scale geothermal potential mapping, West Java, Indonesia.” *Geothermics*, v. 37, n. 3, (2008), p. 267-299.

Crider, , J.G., Frank, D., Malone, S.D., Poland, M.P., Werner, C., and Caplan-Auerbach, J. “Magma at depth: a retrospective analysis of the 1975 unrest at Mount Baker, Washington, USA.” *Bulletin of Volcanology*, v. 73, (2011), p. 175-189.

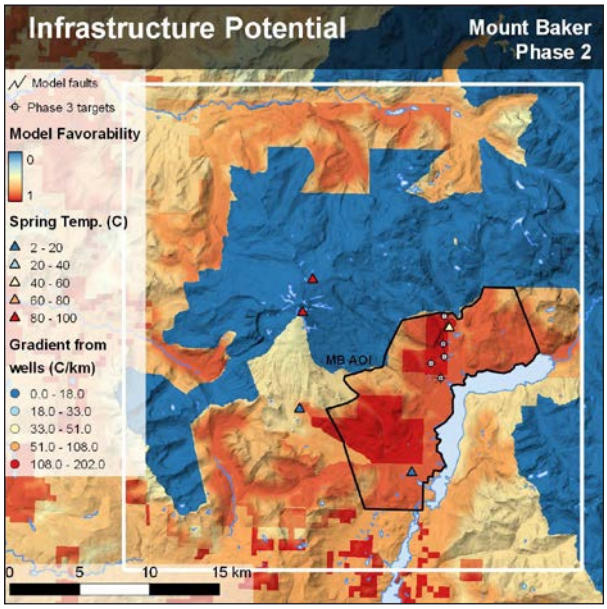

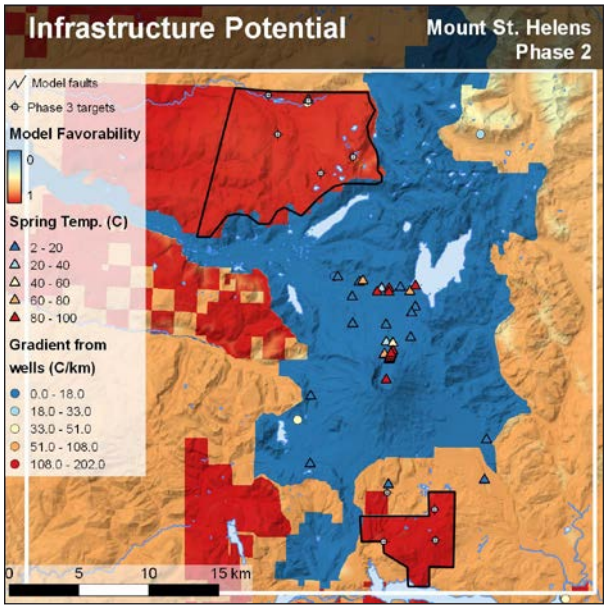

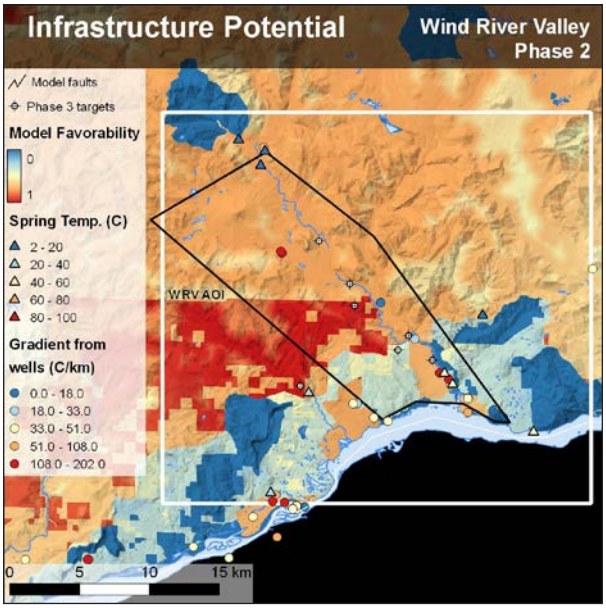

Figure 17. Infrastructure favorability models for all three study areas.

Curewitz, D. and Karson, J.A. "Structural Settings of Hydrothermal Outflow: Fracture Permeability Maintained by Fault Propagation and Interaction." *Journal of Volcanology and Geothermal Research*, v. 79, (1997), p. 149-168.

Czajkowski, J.L., Bowman, J.D., Fusso, L.A., Boschmann, D.E. "Geologic mapping and geothermal assessment of the Wind River Valley, Skamania County, Washington." *Washington Division of Geology and Earth Resources*, Open File Report 2014-01, (2014), 30 p.

Davatzes, N.C., Eichhubl, P., and Aydin, A. "Structural evolution of fault zones in sandstone by multiple deformation mechanisms: Moab fault, southeast Utah." *GSA Bulletin*, v. 117, n. 1-2, (2005), p. 135-148.

DeAngelo, J., Shervais, J.W., Glen, J.M., Nielson, D., Garg, S., Dobson, P., Gasperikova, E., Sonnenthal, E., Visser, C., Liberty, L.M., Siler, D., Evans, J.P., Santellanes, S. "GIS Methodology for Geothermal Play Fairway Analysis: Example from the Snake River Plain Volcanic Province." *Stanford Geothermal Workshop*, (2016).

Eberhart-Phillips, D., Oppenheimer, D. H. "Induced seismicity in The Geysers Geothermal Area, California." *Journal of Geophysical Research: Solid Earth*, v. 89, n. B2, (1984), p. 2156-2202.

Ekström, G., Abers, G.A., and Webb, S.C. "Determination of surface-wave phase velocities across USArray from noise and Aki's spectral formulation." *Geophysical Research Letters*, v. 36, n. 18, (2009).

Evarts, R.C., Ashley, R.P., and Smith, J.G. "Geology of the Mount St. Helens Area: Record of discontinuous volcanic and plutonic activity in the Cascade Arc of Southern Washington." *Journal of Geophysical Research*, v. 92, n. B10, (1987), p. 10,155-10,169.

Evarts, R.C. and Ashley, R.P. "Preliminary geologic map of the Goat Mountain quadrangle, Cowlitz County, Washington." *U.S. Geological Survey*, Open-File Report OF-90-632, (1990).

Fetterman, J.A., and Davatzes, N.C. "Evolution of porosity in fractures in the Newberry Volcano Geothermal System, Oregon, USA: Feedback between deformation and alteration." *GRC Transactions*, v. 35, (2011), p. 339-346.

Fleck, R.J., Hagstrum, J.T., Alvert, A.T., Evarts, R.C., and Conrey, R.W. "$^{40}Ar/^{39}Ar$ geochronology, paleomagnetism, and evolution of the Boring volcanic field, Oregon and Washington, USA." *Geosphere*, v. 10, n. 6, (2014), p. 1283-1314.

Goepel, K.D. "Implementing the Analytic Hierarchy Process as a standard method for multi-criteria decision making in corporate enterprises—A New AHP Excel Template with Multiple Inputs." *Proceedings of the International Symposium on the Analytic Hierarchy Process*, (2013).

Haney, M.M., Mikesell, T.D., van Wijk, K., and H. Nakahara. "Extension of the spatial autocorrelation (SPAC) method to mixed-component correlations of surface waves." *Geophysical Journal International*, v. 191, n. 1, (2012), p. 189-206.

Hole, J. A. and Zelt, B. C. "3-D finite-difference reflection travel times." *Geophysical Journal International*, v. 121, (1995), p. 427–434.

Iovenitti, J., Blackwell, D., Sainsbury, J., Tibuleac, I., Waibel, A., Cladouhos, T., Karlin, R., Isaaks, E., Clyne, M., Ibser, F.H., Callahan, O., Kennedy, B.M., and Wannamaker, P. "Towards developing a calibrated EGS exploration methodology using the Dixie Valley Geothermal System, Nevada." *Proceedings of the 37th Workshop on Geothermal Reservoir Engineering*, Stanford University, Stanford, California, (2012).

Johri, M. "Fault damage zone—observations, dynamic modeling, and implications on fluid flow." *Stanford University PhD Dissertation*, SRB 131, (2012), 194 p.

Lees, J.M. and Wu, H. "Poisson's ratio and porosity at Coso geothermal area, California." J*ournal of Volcanology and Geothermal Research*, v. 95, (2000), p. 157-173.

McCaffrey, R., Qamar, A.I., King, R.W., Wells, R., Khazaradze, G., Williams, C.A., Stevens, C.W., Vollick, J.J., and Zwick, P.C. "Fault locking, block rotation and crustal deformation in the Pacific Northwest." *Geophysical Journal International*, v. 169, no. 3, (2007), p. 1315-1340.

Mignan, A., Landtwing,D., Kästli, P., Mena, B., and Wiemer, S. “Induced seismicity risk analysis of the 2006 Basel, Switzerland, Enhanced Geothermal System project: Influence of uncertainties on risk mitigation.” *Geothermics*, v. 53, (2015), p. 133-146.

O’Connell, R.J. and Budiansky, B. “Seismic velocities in dry and saturated cracked solids.” J*ournal of Geophysical Research*, v. 79, n. 35, (1974), p. 5,412-5,426.

Olmsted, F.H., Glancey, P.A., Harril, J.R., Rush, R.E., and Van Denburgh, A.S. “Preliminary hydrogeologic appraisal of selected hydrothermal systems in northern and central Nevada.” *U.S. Geological Survey*, Open-File Report 75-56, (1975), p. 267.

Olmsted, F.H. “Use of temperature surveys at a depth of 1 meter in geothermal exploration in Nevad.” *U.S. Geological Survey*, Professional Paper 1044-B, (1977).

Personius, S.F., Briggs, R.W., Nelson, A.R., Schermer, E.R., Maharrey, J.Z., Sherrod, B.L., Spaulding, S.A., Bradley, L. “Holocene earthquakes and right lateral slip on the left-lateral Darrington-Devils Mountain fault zone, northern Puget Sound, Washington.” *Geosphere*, v. 10, n. 6, (2014), p. 1482-1500.

Saaty, T.L. “Decision making with the analytical hierarchy process.” *International Journal of Service Sciences*, v. 1, no. 1, (2008), p. 83-98.

Schultz, R.A. “Brittle strength of basaltic rock masses with applications to Venus.” *Journal of Geophysical Research*, v. 98, n. E6, (1993), p. 10,883-10,895.

Shapiro, N.M., and Campillo, M. “Emergence of broadband Rayleigh waves from correlations of the ambient seismic noise.” *Geophysical Research Letters*, v. 31, (2004), L07614.

Stanley, W.D., Johnson, S.Y., Qamar, A.I., Weaver, C.S., and Williams, J.M. “Tectonics and seismicity of the southern Washington Cascade range.” *Bulletin of the Seismological Society of America*, v. 86, (1996), p.1-18

Tabor, R.W., Haugerud, R.A., Hildreth, W., and Brown, E.H. “Geologic map of the Mount Baker 30- by 60-minute quadrangle, Washington.” *U.S. Geological Survey*, Geologic Investigations Series I-2660, (2003).

Thomas, A.L. “*Poly3D* - a three-dimensional, polygonal-element, displacement discontinuity boundary element computer program with applications to fractures, faults and cavities in the Earth’s crust.” *Stanford University Thesis*, Stanford, CA, (1993).

Tibuleac, I.M., Pullammanappallil, S., Faulds, J., and McLachlan, H. “Development of a low cost method to estimate the seismic signature of a geothermal field from ambient seismic noise analysis.” *GRC Transactions*, v. 36, (2012).

Vidale, J.E. “Finite-difference calculation of travel times in three dimensions.” *Geophysics*, v. 55, n. 5, (1990), p. 521-526.

Waite, G.P., and Moran, S.C. “Vp structure of Mount St. Helens, Washington, USA, imaged with local earthquake tomography.” *Journal of Volcanology and Geothermal Research*, v. 182, n.1-2, (2009), p. 113-122.

Wannamaker, P. E., Rose, P. E., Doerner, W., Berard, B., McCulloch, J. and Nurse, K. “Magnetotelluric surveying and monitoring at the Coso geothermal area, California, in support of the enhanced geothermal systems concept: survey parameters and initial results.” *Procedings of the 29th Workshop on Geothermal Reservoir Engineering*, Stanford University, Stanford, CA, (2004).

Weaver, C.S., Grant, W.C., and Shemeta, J.E. “Local crustal extension of Mount St. Helens, Washington.” *Journal of Geophysical Research*, v. 92, no. B10, (1987), p. 10,170-10,178.

Zhu, T.Y. “Some useful numbers on the engineering properties of materials (geologic and otherwise).” *GEOL 615, Department of Geophysics*, Stanford University, Stanford, CA, (2012).